We thank the reviewers for their helpful comments and suggestions. Individual questions and issues are addressed in-line below.

Anonymous Referee #1

General Comments:

1) It is stated that the initial conditions are chosen such that the BL characteristics are in adequate agreement with the observation available 8h into the simulation. Here I would like to be given more detail. In particular it would be interesting to know how strongly the BL characteristics and the roll structures are influenced regarding slight changes in the initial conditions, and how strongly such changes impact your ship track. For instance, as discussed in the paper, the roll structure strongly confines the track if the emissions are set along the roll axes. In particular could the low bias in track width and the smaller simulated roll width be related, and perhaps contribute to the high bias of Nd within the track? Considering the length of the paper, one could consider to present a discussion of the sensitivity to the initial conditions in an appendix.

We agree that the boundary layer is sensitive to the details of the initial conditions, and indeed a series of pilot runs were needed to adjust the geostrophic wind profile and subsidence to achieve a circulation with well-developed roll structure and reasonable agreement with the observed profiles. While the nuanced response of the roll structure to the forcing is an interesting boundary layer dynamics question, the thrust of the paper is to address the aerosol-cloud-precipitation interactions in a case study anchored with aircraft observations, and an extended analysis of the dynamical sensitivities of the initialization and forcing seems a bit outside the scope. The work of Chlond (1992) and Etling and Brown (1993) and references therein provide much more depth on the sensitivities of the roll structure. The LES study of Glendening (1996) provides some insight into the dynamical sensitivities of roll form boundary layers, and has been added as a reference for the interested reader.

2) The aerosol background concentrations and hence background Nd are continuously decreasing with time, as the only source of aerosol, the surface flux, decreases with time. Can you make any statements about the realism of this feature and what causes it? I presume it is linked to the roll circulation, which also reduces in strength as the simulation continues. Could there be issues here, as you consider only one mode of rather large particles? Thereby ignoring any source of particles in the activation range by condensational growth from the Aitken mode as well as new-particle nucleation?

While the Nd value decreases continuously with time after the track is injected at hour 8, it at first increases during the spin up phase when the wind driven surface flux is strong relative to the active removal/dilution processes, which scale with the liquid water path, cloud and rain droplet size spectra, and entrainment rate. At hour 8, when the liquid water profiles and turbulent circulations are most comparable to the aircraft sounding of the background state, aerosol number sink processes most closely balance our parameterized source strength. As our relatively simple model omits nucleation and condensational growth from the Aitken mode, it is possible that this parameterized source strength is unrealistically weak.

Since the aircraft sampled the track for a relatively short period of time, observations do not reasonably constrain the evolution of aerosol number, so it is difficult to say how representative the model behavior is. The results of Mechem et al. (2006) and Berner et al. (2013) suggest that either a large entrainment source (i.e. polluted free troposphere with strong entrainment), which helps to buffer the boundary layer aerosol concentration, or an exceptionally strong surface or nucleation source of aerosol would be needed to balance losses due to collision-coalescence after precipitation strengthens beyond a few mm/day.

3) The discussion of the SensHiAer simulation, although stepping away from the observation, adds scientifically to the paper, as a different ship track behavior is seen in terms of secondary aerosol-cloud interactions. However, the description of the involved processes is not clear yet. Differences in the background state, which behaves differently in terms of LWP and precipitation evolution (Fig. 15), remain largely unexplained. Furthermore, the hypothesized mechanism of the ship track LWP increases one hour after emission is not clear.

Some reorganization of section 5.5 has been done in an effort to clarify the mechanism responsible for the differences in boundary layer organization (suppression of precipitation allowing for a stronger buoyancy flux, more robust rolls, and stronger entrainment), as well as the differing track response (difference in entrainment response dependent on cloud water path and droplet size distribution).

Technical Comments:

1) The symbolism of Na, Nad, Nd is not clearly enough stated at beginning of paper and sometimes mixed up:
- P24424: Nd is used in caption, but Na is used in figure.
- P24395L13: Na used without definition, which follows later in P24399L25.
- In the text Na=Nad+Nd+Nr should always be referred to as total aerosol number concentration and Nad as dry (or maybe unactivated) aerosol number concentration for clarity.

Fixed and clarified as requested.

2) I follow the reasoning for using mg-1 as units of number concentration, but this should be done consistently throughout the paper. If not possible with the observations, I suggest to keep everything in cm-3. Otherwise statements like P24401L8-10 become cumbersome for the reader.

We agree that P24401L8-10 is cumbersome by virtue of the direct comparison between dissimilar units. Throughout the paper, we have made sure like units are always compared. However, we prefer not to convert all the observations to mg^{-1}, as it confuses the issue for anyone referring back to Taylor and Ackerman (1999). In the observational community, it is standard to report Nd and Na in cm^{-3}, while the aerosol modeling community has adopted mg^{-1} for aerosol number; this makes conversions somewhat inevitable when referencing previous work and attempting to maintain readability.

3) P24388L10: change “of cloud” into “of the cloud”.

Changed as requested.

4) P24389L10: Include Christensen and Stephens (2012: Microphysical and macrophysical responses of marine stratocumulus polluted by underlying ships: 2. Impacts of haze on precipitating clouds) in references.

Added as requested.

5) P24393L17: Change "liquid ice static energy" to "liquid static energy".

Changed as requested.

6) P24397L25 and in equation below: Two different values of S are given. Why?

The first value of S is an observational estimate from Hobbs eat al. (2000), the latter is the implied value assumed in the model setup for this paper. We are simply noting that we have chosen a weaker source strength than the previous 1-D version of the case study and believe it to be observationally justified by Hobbs et al. (2000) and Ferek et al. (1998). We have reorganized slightly for clarity.

7) P24398L6-7: Statement unclear.

Rewritten for clarity; we mean that we initially tried the sensitivity test with the same S used in BaseTrack, but the microphysical effects of the perturbation were negligible due to higher background aerosol in the SensHiAer configuration. In order to generate a sufficient microphysical perturbation, we elected to increase the source strength by an order of magnitude.

8) P24398L23: Specify what statistics? Cloud, thermodynamical, dynamical... And change "BaseCtrl, BaseTrack, and SensPerp run suggest" to "BaseCtrl run, and background of BaseTrack and SensPerp

Altered to explicitly assert the similarity of the thermodynamic, dynamical, and microphysical statistics; changed as requested.

9) P24399L23: Mark cross section in Fig.4. If there is a particular reason for choosing 6.4km as cross section location, it should be stated.

Cross section mark added; 6.4km is just the center of the domain, and any other choice would produce a similar result.

10) P24402L17 & P24403L5ff: Fig. 7 suggests that precipitation increases in the track as soon as LWP is increasing. Only when looking at Fig. 15, which is discussed much later, it becomes obvious that drizzle really remains suppressed with respect to the background as LWP increases.

The color scale perhaps makes it difficult to gauge; while light (<1mm day) surface precipitation does redevelop as LWP increases, the pulses of >4mm day rain present in surrounding rolls are essentially absent until after hour 14. Some clarification has been made in the text to address this.

11) P24401L27: I see precipitation change only after 09:30 in Fig.7, which does not add up with 20min given in text.

As above, the first indication of an effect on rain rates is in the loss of the peak surface rain rates in excess of >4mm day. The maximum in the central roll disappears just before hour 9. The description has been amplified to more specifically note this effect, followed by the cessation of virtually all surface precipitation in the central roll after hour 9.5.

12) P24404L25: Tendency of autoconversion is very small. Can that really be taken as evidence?

Sentence rewritten so that the argument does not hinge on the autoconversion tendency. Clearly autoconversion is an important mechanism, since to increase rain rates, more drizzle droplets must be produced (via autoconversion), but the subtle changes in drizzle tendency that drive the later shifts are not readily visible in the time series as presented.

13) P24405L10: Specify that entrainment in track is 3rd largest term. In background its autoconversion.

Corrected as requested.

14) P24407L18: “scaleupdrafts” to “scale updrafts”

Fixed.

15) P24411L15-16: Reformulate. Precipitation is continuously increasing from 9am onwards. It does not start 5h after emission.

Changed to “..reverses five hours after the aerosol injection as increasing precipitation intensity alters the microphysics and entrainment dynamics.”

16) P24416L0-1: Although I agree with your message, I would refrain from speaking about convergence, as the simulations are too short to see real convergence of the curves in Fig.15. For instance panels a1,a3 and b3 of Fig. 15 are clearly not converging in this time period.

“Converging” replaced with “tending” and “convergence” replaced with “approach”.

17) P24417L13-16: Consider breaking up sentence into 2 for readability.

Sentence reorganized for clarity as requested.

18) P24424: Please complete figure caption. ql is not defined and T in caption should be T_abs as in Figure. As mentioned above, there is an inconsistency in notation between Na and Nd.

Caption expanded and details corrected as requested.

19) P24425: In caption write T_abs instead of T.

Changed as requested.

20) P24426: Caption states hour 8, header of Fig. says hour 6. Please change accordingly.

Fixed.

21) P24429: In Fig. Na should be <Na> consistent with caption, where it should be mentioned that <Na> is MBL-depth averaged Na. Also contour spacing of <Na> is not clear.

Caption for Fig. 4 modified to explain depth averaging and for consistency with symbols in Fig. 7; <Na> color scale is quasi-logarithmic, intermediate values added for clarity.

22) P24430: In particular dashed stream lines are hard to identify in bottom panel. Please make it clearer using either larger panels or thicker lines.

Panels enlarged.

23) P24433: A_TOA and A_Cld are not defined in caption.

Definition added to caption.

24) P24434: State scaling of rain mixing ratio in caption.

Changed as requested.

25) P24436: Why are not the same times shown as for Fig.6? It would allow for direct comparison.

While showing the same times would allow direct comparison, the uneven spacing makes it more difficult to gauge the dispersion rate, which is much more rapid in the cross roll case.

26) P24437: panel rows (a), (b), (c) and (d) are swapped between Fig and caption.

Fixed.

27) P24432 and P24439: Replace cyan with different color, as very close to blue when printed.

Changed to orange.

28) P24439: Consider defining RRTM in caption or putting in a reference to the text, where it is defined.

Acronym definition added to the caption.

Anonymous Referee #2

General comments:
It is very interesting to see the simulated mesoscale organization of cloud rolls, for which the formation mechanism is definitely worth exploring. I am sure that the authors must have looked into this, but not much is discussed in the paper. What are the key environmental conditions (e.g., shallow boundary layer, strong winds, large-scale forcing, etc.) for the LES model to produce such cloud rolls? As also noted in the paper, the presence of such roll structures can have a profound influence on turbulent mixing and cloud microphysical processes in the marine boundary layer, compared to the relatively more common open or closed cell structures. Thus the impact of ship emissions on clouds could be quite

different as well. Wang and Feingold (2009b) showed the suppression of cloud formation surrounding the ship track in their drizzling open cell case, which limited the increase of domain average albedo caused by the ship emissions. This suppression effect does not show up in the simulations of this paper. Is this due to some unique mesoscale circulation or cloud dynamics for the cloud rolls? It would be nice to discuss more on this in section 6 in the context of aerosol impact on cloud regime shift.

The focus of our paper is on aerosol-cloud-precipitation interactions as opposed to the nuances of boundary layer dynamics and the observed roll structure. The review of Etling and Brown (1993) extensively covers the details of boundary layer roll dynamics. We have added a reference to the LES study of Glendening (1996), a pioneering example of LES applied to roll form boundary layers. These references together address the environment necessary to generate a roll form boundary layer, as well as the unique dynamical characteristics.

We agree that the effects of ship emissions of clouds in a roll-form boundary layer are indeed likely to be somewhat different than those of other low cloud cellular modes, such as those investigated by Wang and Feingold (2009b), and this is briefly discussed at the end of section 5.6. This is not merely a curiosity, as the study of Durkee et al. (2000a) found that ship tracks are most commonly found in boundary layers with a depth less than 600 m, where roll organization is more common. Our work, in addition to that of Berner et al. (2013), Wang and Feingold (2009b), and others, indicates that the impact of aerosol feedbacks on precipitation and cloud macrophysical properties is strongly dependent on the dominant mode of boundary layer organization, meaning these effects will be difficult to parameterize in larger scale models.

Specific comments and technical edits:

1) P24390, L5-10: it does not seem appropriate to use "positive or negative first/second indirect effect" to describe the increase or decrease of LWP. Reduction of LWP has nothing to do with the conventional aerosol indirect effects. Suggest remove "positive" and change "negative" to something like "opposite to". Same for a few other places throughout the paper.

We are not the first to include liquid water path changes modulated by aerosol-cloud interactions within the second aerosol indirect effect (e.g. Stevens and Feingold, 2009). LWP reductions resulting from aerosol feedbacks on precipitation and macrophysics will necessarily impact cloud radiative forcing and thus constitute an aerosol indirect effect. Albrecht's cloud lifetime effect implicitly requires a link between aerosol and LWP, and this is considered an indirect effect, so it seems artificial to consider more general aerosol-cloud macrophysics feedbacks as very different.

2) P24392, L10: measured by which instrument onboard C-130?

The albedo was measured using the multi-channel radiometer on the C-130. Full instrumentation details are included in Taylor and Ackerman (1999).

3) P24392, L14-17: what's the size range for aerosol particles above cloud? Seems that they are not represented in the bulk aerosol scheme. Also, Nd and Nad (Na in the plot) should be clearly described in the figure caption. Any measurements of interstitial aerosols in the MBL? What is the reason to set initial MBL aerosol concentration substantially smaller than the measured cloud droplet number concentration?

In the case considered, there was negligible aerosol of any size in the region immediately above the cloud. Aerosols entering the marine boundary layer from the free troposphere are generally smaller than the accumulation mode and thus not explicitly represented within our model. In previous work, we simply considered the particles entering the boundary layer via entrainment to instantaneously grow via condensation into viable CCN in order to avoid the complexities of multiple aerosol modes. While this ignores potentially important aerosol mechanisms and the time lags associated with their action, it still appears to be a useful approximation.

Nd and Nad are now defined in the figure caption. Interstitial aerosol measurements in the boundary layer were not available, as the C130 instrumentation included PCASP, FSSP, and 2-DC probes. The PCASP, which sizes smaller aerosols, suffers from droplet shattering artifacts within cloud, so in-cloud interstitial retrievals are not possible. Furthermore, the C-130 was unable to fly below cloud during the observations due to the extreme low cloud base, so it was not possible to reliably examine interstitial aerosol in the boundary layer in the case studied here.

The initialization of the boundary layer aerosol to a lower value was done as part of the tuning process. Because it takes the model some time to develop the boundary layer cloud and roll structure, the parameterized surface aerosol flux increases the boundary layer aerosol number concentration over the first few hours, and starting at this lower initial value then yields the approximately observed conditions once the cloud rolls and turbulence are fully developed.

4) P24394, L1: change “precipitation” to “raindrop”. Having Lookup table for cloud droplet sedimentation as well?

Changed as requested; cloud droplets fall velocities are also obtained from a lookup table.

5) P24394, L11 and L15: no need to use “dry” to describe aerosols, which usually take up water to various extents.

Changed as requested.

6) P24394, L20: not quite clear why such a high model top (29km) is needed for the radiation schemes when using diurnally averaged radiative forcing in the simulations. I assume that the sounding does not cover to that height. What profiles are used then?

The sounding above the C-130 profile was inferred from ERA-Interim reanalysis. While the radiation is diurnally averaged, it still includes a full shortwave and longwave radiation calculation from RRTM. The version of the radiation code used with the build of SAM used in our study did not easily handle a truncated vertical domain, so it was simplest to extend the domain rather than reengineer the radiation code.

7) L24396, L4-5: Could the “large scale updraft” be verified from reanalysis? I am wondering how strong a large-scale lifting can really affect droplet nucleation.

We have reworded this sentence for clarity, replacing “large scale” with “mesoscale”; the intended meaning is that the C-130 profiled through the updraft between boundary layer rolls that forms the cloud bands, not large scale in the sense of anything resolved by reanalysis.

8) L24396, L25: please describe how the divergence was converted to subsidence and used in the model.

Constant divergence from 3000m to the surface implies a linear subsidence profile. This is applied as a large scale nudging tendency on scalar fields

9) P24397, L11: which scheme is used to parameterize surface salt fluxes? Only the accumulation mode is accounted for?

We use a modified form of the Clarke et al. (2006) flux parameterization which accounts for only the accumulation mode contribution that constitute immediately viable CCN; this is briefly mentioned in section 3.

10) P24397, L15: “m” is missing in the units of radius.

Fixed.

11) P24397, L28: please verify if S = 2.3e16 or 1.5e16. The former is inconsistent with the value given in L15, and does not seem to give s=15000 per mg.

The reviewer is correct; on examining our original calculation, we used an f_{CCN} of 0.08, which combined with the air density 1.2 kg m^{-3} from the initial conditions implies S = 2.3e16 s^{-1}. On reexamining Hobbs et al. (2000), f_{CCN} is estimated at 4% to 18% for a range of ships similar to the *Sanko Peace* burning marine fuel oil, with aerosol flux estimates ranging from 4.5e15 s^{-1} to 1.5e16 s^{-1} for the four ships where detailed estimates were made. Ferek et al. (1998) suggested an initial f_{CCN} of 10% that may increase over time with plume dilution. At any rate, the aerosol initialization selected for the plume in our model is compatible with the observational estimates of similar ships, and does not seem unreasonable given the substantial uncertainty.

12) P24398: would be nice to have all simulations summarized in a table.

Since we present only four simulations, which are described at the beginning of Sec. 5, we feel a table of runs is unnecessary.

13) P24399, L11: no need to have “Cloud” here

Changed as requested.

14) P24399, L25: “unactivated, interstitial” is redundant and a little confusing. Suggest remove “unactivated”

Changed as requested.

15) P24400, L11: It seems that the albedo here is not just for the visible wavelengths. How accurate are the equations (2 and 3) and associated parameters for the entire SW spectrum? Does the underlying ocean surface have zero albedo?

The albedo as described on P24400 refers to one deduced from the RRTM SW calculation. The shortwave flux partitioned in the RRTM calculation includes a component outside the visible spectrum, but as the bulk of the flux is at visible wavelengths, this seems a reasonable approximation.

16) P24400, L25-26: unclear about "the scale" in Figure 6.

Reorganized for clarity; the scale discussed in lines 25-26 is that on the Hovmoeller plots in Fig. 7.

17) P24402, L22-27: Is there a physical explanation why the results are different from those seen in previous studies?

We expect that the lack of suppression hinges on the significant differences in the turbulent organization of the boundary layer. The turbulent circulations in a roll-form collapsed boundary layer are driven in part by wind shear, while the cellular circulations considered by Wang and Feingold (2009b) are driven by buoyancy flux and cold pool dynamics. It may be that the strength of the secondary circulation generated by changes in precipitation and hence cold pooling are much weaker relative to the shear driven flow, whereas in an open cell circulation the secondary flow is comparable in strength, but this is speculation.

18) P24406, L14-15: why lower cloud cover results in a low bias in Nd? Isn't the Nd averaged in clouds?

The transects presented are y-averaged. Because of variability in cloud cover and horizontal gradients in cloud droplet concentration, cloud conditional averaging can produce misleading artifacts. For simplicity we have used a domain y-average at the sampling level. This has been clarified in the text.

19) P24408, L24: the "360 minutes" after track injection (hour 8) does not match the "hour 15" in the figure.

The figure caption is correct; text amended to 420 minutes.

20) P24415, L7: typo for "occur"

Fixed.

21) P24417, L7: scavenging "of" interstitial aerosol?

Changed as requested.

22) P24425, Figure 3: What does the "large scale" mean here? Why don't use simulated vertical velocities instead of LWP for the conditional sampling?

"Large scale" is meant to refer to the lateral length-scale of the mesoscale rolls. Sampling is done by LWP as it seemed to yield slightly cleaner sampling than the vertical velocity in a y-average.

23) P24426, Figure 4: “hour 6” or “hour 8” in the title of the albedo panel? Strictly speaking, the plots must be from the run BaseSpinup rather than BaseTrack (said in the caption) as ship track does not appear in the albedo plot yet.

The title is incorrect—the frame is from the beginning of hour 8, and the title has been changed accordingly. The frame shown is the first frame of run BaseTrack, as the shiptrack is injected 30s after the run is branched from the end of BaseSpin.

24) P24427, Figure 5: also for run BaseSpinup? Please describe the white (cloud) contours in the figure caption. Why they look so different in the two panels?

The white contour marks the 0.01 g kg-1 cloud water boundary. The difference in appearance is due to the y-averaging of the fields in the upper panel, while the lower panel is a slice across the middle of the domain. The caption has been altered for clarity.

25) P24431, Figure 9: why domain-average Nd is shown rather than cloud-average?

Cloud fraction varies strongly with height, and a cloud conditional average would only average over the updraft bases, while higher in the profile would average across cloud in the updraft and updraft. Rather than add multiple layers of conditional sampling, it seemed simplest to average across the domain.

26) P24432, Figure 10: suggest change “sinks” in the titles to “budget” since sources are plotted too. Are these terms averaged within the boundary layer?

Changed to “boundary layer averaged budget”.

27) P24434, Figure 12 caption: change “times” to “hour” and add the experiment name.

Changed as requested.

28) P24437, Figure 15: remove units in the third row, as the quantity is not number concentration anymore.

Fixed.

Manuscript prepared for Atmos. Chem. Phys. Discuss.
with version 4.0 of the LaTeX class copernicus_discussions.cls.
Date: 2 April 2015

Large-Eddy Simulation of Ship Tracks in the Collapsed Marine Boundary Layer: A Case Study from the Monterey Area Ship Track Experiment

A. H. Berner[1], C. S. Bretherton[1], and R. Wood[1]

[1]Department of Atmospheric Science, University of Washington, Seattle, Washington

Correspondence to: Andrew Berner
(andy.berner@gmail.com)

Abstract

For the first time, a large-eddy simulation (LES) coupled to a bulk aerosol scheme is used to simulate an aircraft-sampled ship track. The track was formed by the M/V *Sanko Peace* on June 13, 1994 in a shallow drizzling boundary layer with high winds but very low background aerosol concentrations (10 cm^{-3}). A Lagrangian framework is used to simulate the evolution of a short segment of track as it is advected away from the ship for eight hours (a downwind distance exceeding 570 km).

Using aircraft observations for initialization, good agreement is obtained between the simulated and observed features of the ambient boundary layer outside the track, including the organization of the cloud into mesoscale rolls. After eight hours, a line of aerosol is injected to start the ship track. The simulation successfully reproduces the significant albedo enhancement and suppression of drizzle observed within the track. The aerosol concentration within the track dilutes as it broadens due to turbulent mixing. A sensitivity study shows the broadening rate strongly depends on the alignment between the track and the wind-aligned boundary layer rolls, as satellite images of ship tracks suggest. Entrainment is enhanced within the simulated track, but the observed 100 m elevation of the ship track above the surrounding layer is not simulated, possibly because the LES quickly sharpens the rather weak observed inversion. Liquid water path within the simulated track increases with time even as the ambient liquid water path is decreasing. The albedo increase in the track from liquid water and cloud fraction enhancement (second indirect effect) eventually exceeds that from cloud droplet number increases (first indirect or Twomey effect). In a sensitivity study with a higher initial ambient aerosol concentration, stronger ship track aerosol source, and much weaker drizzle, there is less liquid water inside the track than outside for several hours downwind, consistent with satellite estimates for such situations. In that case, the Twomey effect dominates throughout, although, as seen in satellite images, the albedo enhancement of the track is much smaller.

1 Introduction

Ship tracks are one of the most striking examples of anthropogenic impact on the atmosphere. Conover (1966) first identified ”anomalous cloud lines” over the ocean in early visible-wavelength satellite imagery. He correctly hypothesized that cloud condensation nuclei (CCN) forming in plumes of ship emissions could perturb marine boundary layer (MBL) clouds and increase their reflectance. Twenty years later, Coakley et al. (1987) found that many ship tracks without an obvious visible-wavelength albedo signature could still be detected using near infrared (IR) satellite imagery, because of the sensitivity of near-IR radiative transfer to the cloud droplet size spectrum. Later work (Coakley and Walsh, 2002; Chen et al., 2012; Christensen and Stephens, 2012) deduced liquid water path (LWP) changes between ship tracks and the surrounding environment, showing that tracks could also exhibit LWP decreases, not just LWP increases.

The effects of aerosols on cloud radiative properties are often partitioned into the first (Twomey, 1977) and second (Albrecht, 1989; Liou and Ou, 1989; Stevens and Feingold, 2009) aerosol indirect effects. The first indirect effect is the change in net top-of-atmosphere (TOA) shortwave radiation (positive downward) resulting from a change in cloud droplet number when holding other properties constant, while the second aerosol indirect effect is the additional net TOA shortwave change due to impacts on macrophysical cloud properties like water content, precipitation, turbulence and cloud lifetime that result from microphysical feedbacks. Ship tracks owe their existence to aerosol-cloud interactions, and thus provide an excellent means to study them.

The first in-situ measurements of ship tracks were made with an aircraft by Radke et al. (1989) in a solid stratocumulus deck, and from a ship by Hindman et al. (1994) under cleaner conditions with a lower background cloud fraction. Ackerman et al. (1995) used these observations as the basis for a modeling study. They classified ship tracks as ‘Type 1’, with an obvious albedo enhancement in visible satellite imagery, or ‘Type 2’, evident only in near-IR (3.7 μm) images. They employed a one-dimensional column model with a turbulence closure, which is a computationally efficient way to focus on aerosol-cloud interaction but has limited scope, since it cannot simulate horizontal dispersion, the circulation structure of a ship track, or horizontal covariations between turbulent eddies and cloud throughout the boundary layer. In their simulations of the Type 1 track (based on the observations of Hindman et al., 1994), LWP and cloud droplet number concentration N_d were elevated above the control run for the entirety of the simulation (a positive first and second aerosol indirect effect), yielding a substantial increase in albedo (greater than 50%). They also simulated a Type 2 ship track (based on the observations of Radke et al., 1989) and found a daytime LWP reduction (negative second aerosol indirect effect), due to enhanced subcloud drizzle evaporation giving a less well-mixed boundary layer. These results compared reasonably well to the limited available observations.

Community interest in aerosol cloud interactions as exemplified by ship tracks led to the Monterey Area Ship Track experiment (MAST; Durkee et al., 2000) in 1994. Aircraft surveys by multiple platforms provided in-situ measurements of many ship tracks and their contrast with the ambient boundary-layer conditions. During research flight A338 on June 13th, 1994, the United Kingdom Meteorological Office (UKMO) Meteorological Research Flight (MRF) C-130 sampled a Type 1 ship track generated in a collapsed boundary layer by the M/V *Sanko Peace*. Arguably, this is one of the best-sampled Type 1 ship tracks documented in the scientific literature. An interesting and unusual feature of the case was the observation that the ship track appeared elevated as much as 100 m above surrounding cloud tops. Taylor and Ackerman (1999) summarized the extensive set of aircraft measurements and performed comparison simulations using their 1D column model. They obtained good agreement with the relative albedo enhancement seen in the observations, with comparable LWP, effective radius r_e, and N_d in both the track and background environment, but again their modeling framework was not designed to simulate the horizontal structure of the track and its downstream evolution.

An obvious step up in modeling sophistication would be to use a large eddy simulation (LES) coupled to an aerosol physics model. Surprisingly few LES of real ship tracks have been attempted. The studies of Wang and Feingold (2009b) and Wang et al. (2011) examined idealized ship tracks in an 800 m deep boundary layer, at the upper limit of the 300–800 m MBL depth range typical of the MAST cases (Durkee et al., 2000a). Their simulated tracks showed regions of albedo reduction around the ship track that in area-mean largely cancelled out the enhanced in-track albedo, yielding a very weak total aerosol indirect effect. However, they had no observational constraint, a limitation that the present study aims to address.

We revisit the *Sanko Peace* case using an LES model with a coupled bulk aerosol model developed by Berner et al. (2013). The case provides an opportunity to test the skill of this model, which combines a sophisticated representation of turbulence with an intermediate-complexity description of the aerosol and its interaction with cloud processes, against observations, and more generally test whether this modeling framework can significantly add to one-dimensional turbulence closure methods. Our work is organized as follows: further detail on the observations and previous modeling work is given in Sec. 2. Model formulation is described in Sec. 3 and forcing and initialization detailed in Sec. 4. The simulations are discussed in Sec. 5, including sensitivity studies on track orientation and background aerosol concentration, and a simplified model for cloud albedo (Platnick and Twomey, 1994; Brenguier et al., 2000) is used to partition the simulated albedo enhancement into contributions from the first and second indirect effects. In Sec. 6, we briefly discuss the interpretation of the simulations in the context of cloud-aerosol regimes (Rosenfeld et al., 2006; Berner et al., 2013), followed by conclusions in Sec. 7.

2 The Sanko Peace case study

Our case study description draws from the work of Taylor and Ackerman (1999), additional analysis of the flight data (kindly provided by Simon Osborne of the UKMO), and satellite imagery for the case. For details of the aircraft instrumentation and sampling strategy, the interested reader is referred to the Taylor and Ackerman (1999) study. The boundary layer was quite shallow, with cloud tops at 300 m and very clean background aerosol concentrations of 10 cm^{-3}. CCN and condensation nuclei (CN) concentrations were negligible above the inversion up to a kilometer in depth. MBL wind was moderately strong, with aircraft observed speeds of $\sim$14 m s^{-1} (150 m altitude) from the north-northwest, driving coherent roll structures within the boundary layer (for a review of boundary layer roll vortices, see Etling and Brown, 1993). We obtained Geostationary Operational Environmental Satellite (GOES) visible imagery at the time of aircraft sampling, which is shown in Fig. 1. The roll organization within the boundary layer is readily apparent; unfortunately, high cirrus cloud obscured the boundary-layer clouds near the coast, making it difficult to discern the track, despite a 35% increase in peak albedo measured by the C-130's multi-channel radiometer. The right-hand panel gives an enlarged view of the region near Monterey, and the heads of several faint tracks mentioned in the flight notes are identified with arrows. A solid arrow marks the estimated location of the *Sanko Peace*, established based on image time and GPS coordinates from the aircraft.

Fig. 2 shows an aircraft profile of the environmental wind, liquid water content q_l, total water q_t, cloud droplet concentration N_d (in cloud) and unactivated aerosol concentration N_{ad} (above cloud; for instrumentation details, see Taylor and Ackerman (1999)), and absolute temperature T_{abs} (black curves), with overlaid geostrophic wind forcing and idealized initial profiles (blue curves, discussed below in Sec. 4). The inversion structure is quite distinctive, with three nearly isothermal layers, each $\sim$100 m in depth, separated by 2–3 K inversions. These layers are all quite moist, with q_t values of 9.25–10 g kg^{-1}, nearly identical to the well-mixed layer below. While N_d in the cloud varies between 25–30 cm^{-3}, the air in the 100 m layer above is essentially pristine, with negligible N_{ad}, and only small concentrations above up to 1 km (10–30 cm^{-3}, of which a large portion is likely at the smaller end of the size spectrum). This structure could reflect differential advection in layers above the inversion base. It is also suggestive of the result of an aerosol-cloud-precipitation feedback-induced collapse of a deeper boundary layer (Ackerman et al., 1993), in which the secondary inversions mark the subsided locations of previous stratocumulus layers which became too optically thin to drive sufficient turbulence to sustain themselves.

Taylor and Ackerman (1999) reported that the ship track rapidly deepened by 100 m above the surrounding background cloud in less than an hour of downstream development. This rapid deepening may have been partially enabled by the weak cloud-top inversion, but their simulation, which idealized the observed profile, did not produce nearly as much deepening as was observed. Recent remote sensing studies have shown deepening of Type 1 ship tracks to be relatively common (Christensen and Stephens, 2011), but almost no other in-situ profiles of the environments that support such deepening are available.

3 Model formulation

In the present work, simulations are performed using the System for Atmospheric Modeling (SAM) version 6.9 (Khairoutdinov and Randall, 2003). SAM uses a dynamical core formulated on the anelastic approximation to the Navier Stokes equations to represent fluid motion resolved on the grid. The effects of subgrid turbulence are handled using the 1.5 order turbulent closure model of Deardorff (1980). Scalar advection is performed using the piecewise parabolic method of Blossey and Durran (2008). Coriolis force is included using an f-plane approximation, with the Coriolis parameter specified appropriately for the latitude of the case considered. Liquid static energy, $s_l = c_pT + gz - Lq_l$, is the conserved thermodynamic variable, as the ice phase is not present in the warm rain cases under consideration. Here c_p is the isobaric heat capacity of air, g is gravity, z is height, L is the latent heat of vaporization, and the liquid water mass mixing ratio q_l is the sum of cloud water (drops smaller than 25 micron radius) q_c and rain water (drops larger than 25 micron radius) q_r. Water vapor q_v is advected separately, and condensation is calculated by saturation adjustment. Surface fluxes are calculated in each grid from Monin-Obukhov theory.

Microphysical tendencies are calculated using the two-moment Morrison scheme (Morrison and Grabowski, 2008; Morrison et al., 2005) with the precipitation parameterization of Khairoutdinov and Kogan (2000). A number of modifications have been made, including the use a lookup table for cloud droplet sedimentation and raindrop fall speeds, rain evaporation, and the shape parameter for the gamma rain distribution.

A simple bulk aerosol scheme (described in Berner et al., 2013) has been coupled to the microphysics. It predicts mass and number for a single accumulation mode with a log-normal size distribution of aerosol number that has an assumed geometrical standard deviation $\sigma_g = 1.6$. This approach requires a minimal number of additional advected scalars while allowing for the inclusion of realistic aerosol-cloud-precipitation feedbacks; a limitation of this method is that it does not represent the growth of a separate Aitken mode of smaller particles to CCN-active sizes. Processes affecting aerosol in the scheme include activation, autoconversion, accretion, evaporation, scavenging of interstitial unactivated aerosol by cloud and rain, and fall-out to the surface. A surface source based on the sea-salt parameterization of Clarke et al. (2006) is included. Radiation calculations are performed using the Rapid Radiative Transfer Model (RRTM; Mlawer et al., 1997), which in our implementation utilizes a combined cloud-drizzle r_e diagnosed from the 3D microphysical fields. Unactivated aerosol is not included in the radiation calculation.

3.1 Model domain, resolution, and boundary conditions

Simulations in this paper are run on a 51.2 km×12.8 km domain with 50 m horizontal resolution. Vertical spacing is 15 m near the surface, shrinking to 5 m in a layer from 70 m to 500 m in depth, and then stretching continuously to the domain top at 29 km (necessary to avoid reengineering the implementation of the radiative transfer scheme in the model). The time step is 0.5 seconds. Boundaries are doubly periodic in the horizontal, with a sponge layer in the upper portion of the domain to absorb gravity waves and prevent spurious reflections from the rigid lid.

4 Initialization and forcing

The goal of our model initialization and forcing is to produce a boundary layer qualitatively and quantitatively similar to the background environment described by Taylor and Ackerman (1999). As the evolution of the boundary layer prior to sampling and large scale meteorological forcings remain uncertain, the final initial values and forcings were empirically chosen using pilot simulations to improve the quantiative match between observations and the hour eight boundary layer statistics.

4.1 Temperature, moisture, and wind

The horizontal coordinates x and y are aligned such that the boundary-layer mean wind, which is from 30° west of north, lies along the $-y$ direction. u and v denote the wind components in the x and y directions. The blue curves in Fig. 2 show the geostrophic wind profiles U_g and

V_g used to force the model, which were chosen to produce approximately the observed wind profiles, as well as the smoothed q_t, total aerosol concentration N_a, and T profiles used for model initialization. The initial q_l profile is diagnosed from saturation adjustment; N_a is the sum of interstitial aerosol N_{ad}, cloud droplets N_d, and rain N_r.

In Fig. 3, red and blue curves show y-averaged profiles of u and v, liquid water mass mixing ratio q_l, q_t, absolute temperature T_{abs} and cloud droplet concentration N_d for updrafts and downdrafts from the control run at hour eight, overplotted with the aircraft observations (black curves). The coherent roll organization of the boundary layer results in considerable differences in wind shear, q_l, and N_d between the roll-scale updrafts and downdrafts. For instance, wind speeds are 2–3 m s^{-1} faster in the downdrafts, since surface drag decelerates the flow before it ascends in the updrafts. Total water content in the updrafts is substantially larger than the downdrafts, reflecting the strong precipitation within the updrafts and broader downdraft regions. The initial stair-step temperature structure above the inversion has been mixed/diffused out after eight hours. If the observed structure results from the boundary layer collapse process discussed in Ackerman et al. (1993), this suggests that the model is too diffusive in the region above the inversion or perhaps allows mixing not present in the real case. Alternatively, the observed structure may result from layered advection.

Since the observed wind shear at cloud top is large and N_d is at the upper end of the observational range, it is likely that the aircraft profiled through the center of a roll-scale updraft. The forcing parameters and initial conditions have therefore been tuned to match the mean updraft structure after the eight hours, when the roll vortices are fully developed and the ship track is inserted.

Because of the low cloud base, the C-130 could not radiometrically observe the SST. Taylor and Ackerman (1999) used a sea surface temperature (SST) of 287 K; in our pilot simulations, the T_{abs} and q_l profiles matched observations better with an SST of 288 K, so that is used here. With our choice of geostrophic wind profile and SST, the final updraft profile matches the observations reasonably well, though the inversion jumps are smeared somewhat by averaging due to variations in cloud top along the y-axis.

4.2 Radiation

Since the observations are inadequate to resolve temporal evolution of the other meteorological forcings in this case, radiative forcing is diurnally averaged. The model uses an insolation-weighted solar zenith angle appropriate to the date and latitude (June 13, 34° N).

4.3 Subsidence

A constant divergence assumption is applied from 3000m to the surface, implying a linear subsidence profile which acts as a large-scale forcing on the thermodynamic and microphysical fields. Accurate divergence measurements are quite difficult to obtain from observations; ERA-interim reanalysis (Dee et al., 2011) values for subsidence are quite variable in space and time along the coast of Southern California for the *Sanko Peace* case. We used an empirically determined divergence of 6.4×10^{-6} s^{-1}, which maintains a realistic and fairly constant MBL height through the majority of the simulation.

4.4 Microphysics

The initial MBL aerosol concentration is set to 10 per mg dry air for the baseline case. Aerosol concentrations given in these units are conserved for adiabatic parcel motions, and thus preferred. This is comparable to the mean N_d reported by Taylor and Ackerman (1999) (their values are reported in units of cm^{-3}, which are roughly 30% larger than values in units of mg^{-1} within the shallow boundary layer; this comparison also assumes that in the model, most aerosol will be activated in updrafts, which holds for the simulated conditions). The initial geometric mean radius of the aerosol is chosen as 0.1 μm. Free tropospheric aerosol is set to zero, as aircraft observations showed negligible CN/CCN above the inversion. Thus the only supply of aerosol to the cloud layer is from the parameterized surface salt flux, which is large due to the high wind.

After eight hours of simulation, we branch off a ship track run. To represent the track, the aerosol concentration between $z = 0 - 100$ m in a single line of grid columns down the center of the domain along the y-axis is instantaneously set to $s = 15000\ \mathrm{mg}^{-1}$, with a geometric mean radius of 0.1 μm. This approach is an approximation to the emissions from a ship steaming into the low-level wind. It would be more realistic to insert the aerosol at a location that follows the ship motion, but given the ship relative wind-speed $V_{rel} = 20\ \mathrm{m\,s}^{-1}$, the track would take only 10 minutes to advect across the 12.8 km length of the domain in the y direction. Our initialization procedure makes the track evolve similarly at all y, allowing us to conveniently use y-averaging to robustly characterize the overall track evolution. The track simulation is continued for another eight hours. For comparison, we also continue the control run with no added ship emissions.

We justify our choice of s as follows. First, we link the grid perturbation s and the implied aerosol source strength S. Given the perturbed depth h = 100 m, horizontal grid spacing Δx of 50 m, air density ρ_a of 1.2 kg m^{-3}, and fraction of viable CCN f_{CCN} set to 0.15,

$$s = f_{CCN} S/(\rho_a h \Delta x V_{rel}) = 15{,}000\ \mathrm{mg}^{-1} \rightarrow\ S = 1.2 \times 10^{16}\mathrm{s}^{-1}. \quad (1)$$

Taylor and Ackerman (1999) performed their 1D simulation of the *Sanko Peace* with an implied S of 3.0×10^{16} s^{-1}. They based their choice on the aerosol measurements of the *Cosco Tai He*, described in Hobbs et al. (2000). Their implied source was twice the strength of the upper bound derived in Hobbs et al. (2000), done in order to counteract the underprediction of supersaturation (and thus activation) in their model. Since the aerosol scheme used in our study only includes the accumulation mode, we further need to assume a value of f_{CCN}. Ferek et al. (1998) found that 10-30% of particles emitted are initially activated, while increasing supersaturation over time could contribute to increased activation downstream, along with the possibility of further CCN production via gas deposition growth of Aitken mode particles to CCN active size. Aircraft measurements reported by Hobbs et al. (2000) estimated the initially activated fraction in a range from 4-25% with significant variation between the different ships sampled, with an estimate of 8% for the *Cosco Tai He*.

While the activation scheme in our model (Abdul-Razzak and Ghan, 2000) has some capability to capture changes in activation due to variations in updraft strength, the growth of smaller particles to CCN active sizes is neglected. Assuming a larger value for f_{CCN} of 0.15 to roughly approximate the growth of CN to CCN downstream, our value of S is 1.2 $\times10^{16}$

s^{-1}, in line with the Hobbs et al. (2000) measurements for the *Cosco Tai He*. The *Sanko Peace* is a smaller ship, so the analog is not perfect, but the above calculations suggest our source strength is reasonable. We also perform a high-aerosol sensitivity study with an initial background boundary-layer aerosol concentration of 300 mg^{-1}. In an initial pilot simulation with the same source strength as in control simulation, the plume rapidly diluted with minimal microphysical or macrophysical impact. In order to observe a clear signal, we increase the amplitude of the source by a factor of ten for the high-aerosol case.

5 Simulations

Four simulations will be discussed. Run BaseSpinup is the starting point for our study, in which an initial sounding adapted from the ambient C-130 vertical profile preceding sampling of the *Sanko Peace* track is spun up for eight hours, at which time the model evolution agrees reasonably well in a quantitative sense with observations of the key thermodynamic and microphysical variables. At this point, the simulation is branched into runs BaseTrack, in which an aerosol perturbation representing the shiptrack is inserted, and BaseCtrl, which is left unperturbed; both branches are evolved for a further eight hours. Two sensitivity studies are also performed. In run SensPerp, wind forcing is rotated 90° clockwise to orient the rolls parallel with the longer x dimension of the domain; the aerosol perturbation is now perpendicular to the roll structure, resulting in more rapid turbulent diffusion through the boundary layer. Lastly, run SensHiAer enhances the background aerosol concentration and that of the ship track perturbation as described in Sec. 4.4 above. Both sensitivity runs spin up for eight hours, at which point the tracks are inserted and evolved for an additional six hours. Thermodynamic, dynamical, and microphysical statistics of the BaseCtrl run are nearly identical to those sampled from the background regions of the BaseTrack and SensPerp runs, suggesting that BaseCtrl is an adequate control for run SensPerp. A comparison between the general statistics of BaseCtrl and the out-of-track background environment in BaseTrack suggests that sampling of the background for SensHiAer provides an adequate control for that case, so separate control branches for the sensitivity runs are not performed.

5.1 Background environment

We begin by examining the evolution of the unperturbed background environment in BaseSpinup. Roll structures develop almost immediately, with a cross-axis length scale of a few hundred meters, growing to approximately 1.7 km at hour four and 2.5 km at hour eight. Fig. 4 shows $x-y$ plots of albedo, MBL depth averaged aerosol number, LWP, and surface precipitation intensity. The albedo plot strongly resembles the GOES imagery in the enlarged panel of Fig. 1 and other similar roll-organized boundary layers. The modeled roll wavelength is smaller than the approximately 5 km scale in the satellite imagery, which we attribute to the continued upscale evolution of the real boundary layer vs. an eight hour spin-up from rest in the model.

LWP and albedo maxima (minima) mark the updrafts (downdrafts). Despite the very shallow boundary layer, LWP averages $\sim$100 g m^{-2} in the updrafts, with maxima exceeding 150 g m^{-2}. Cloud base beneath the updrafts is mostly at the surface. While there are large variations in albedo in the cross-roll direction, domain cloud cover is quite high ($\sim$87.5% at hour eight, based on a 10 g m^{-2} minimum cloud water path (CWP) threshold). Aerosol number concentrations are 25–30 mg^{-1} in the updrafts, where air recently in contact with the surface source is converged, while downdraft air is aerosol-depleted ($\sim$10 mg^{-1}) due to collision-coalescence losses in the clouds and mixing with the pristine air entrained from above. Domain average surface precipitation is 0.5 mm day^{-1}, but locally, precipitation is up to 6 mm day^{-1} in narrow regions beneath the updrafts with highest LWP, and such rain bands contribute a significant fraction of the mean precipitation.

Fig. 5 shows an x-z snapshot at hour eight of the y-averaged vertical velocity and a slice of total aerosol number concentration N_a taken across the domain at y = 6.4 km. For reference, the cloud contour q_c = 0.01 g kg^{-1} is also shown. In the simulation, a small amount of aerosol detrains in the layer immediately above the rolls as a result of evaporation and mixing. The observations had essentially no aerosol above cloud top (with one exception discussed below in Sec. 5.3), suggesting the model may again be slightly too diffusive with the very sharp vertical gradient in the aerosol field. Typical peak vertical velocities in the updrafts are 0.5–0.8 m s^{-1} in very narrow bands of $\sim$200 m wide (variations in the updraft position along the roll diminish this when averaging in y). The w-slice also shows that the downdrafts are considerably broader than the updrafts.

5.2 Ship track injection and evolution

In this section, we analyze branch BaseTrack and compare it to the unperturbed BaseCtrl. The albedo A is computed in each column from the TOA downwelling and upwelling shortwave radiative fluxes,

$$A = SW_{\uparrow}^{TOA} / SW_{\downarrow}^{TOA}$$

Fig. 6 shows the albedo A at 0.5, 1.5, 3.0, and 8.0 hours after the aerosol injection, which is initially below a roll-scale updraft, producing a sharp, bright albedo signature which diffuses with time. For most of the following discussion, we consider Hovmöller plots of the salient fields, interpreting downstream distance as the time after injection multiplied by the 20 m s^{-1} ship-relative wind speed. Plots of albedo and surface precipitation use data output once a minute from the model, and are formed by combining transects at $y = 6.4$ km from all times. Calculation of the $< N_a >$ and LWP fields required data available in the 3D outputs once every 10 minutes. In order to better represent the variability of these fields, we subsitute spatial resolution for time resolution of these variables by sequentially cycling through transects at each of the 10 y locations nearest y=6.4 km for each 3D output, yielding the same number of transects for all fields. Note that these plots present a highly compressed view of the along-track direction, in that the 8 simulated hours correspond to a downstream distance of 576 km, given the 20 m s^{-1} ship-relative surface wind speed, while the cross-track domain width is 48 km. The right-hand axis of panel (d) in Fig. 7 and Fig. 16 shows equivalent downstream distance.

The albedo of unbroken stratocumulus clouds can be related to their cloud droplet concentration (which is in turn related to $< N_a >$) and LWP; the relative importance of N_d and LWP contributions to the track albedo response is explored in Sec. 5.6. Fig. 7 shows a Hovmöller plot of the time evolution of albedo, $< N_a >$, LWP, and surface precipitation.

At 30 minutes after injection, the ship track aerosol has been laterally mixed across slightly more than 1 km, diluting the initial concentration from an MBL depth-averaged value of 5000 mg^{-1}

to values between 100–325 mg^{-1}. Assuming nearly complete activation (as is simulated in this case) and a vertically well-mixed profile, this gives a peak N_d of 420 cm^{-3} at 300 m altitude, a value nearly four times larger than observed in an observational transect sampled 30 min downstream of the ship (Taylor and Ackerman, 1999). Imperfect alignment of the ship's course and the roll axis may have led in reality to more rapid turbulent diffusion of the aerosol than in the simulation. Consistent with this hypothesis, the observed track width of 4 km is four times as large as the simulated width. Sec. 5.3 further discusses of how track orientation affects track width. Other possibilities are that the effective aerosol injection strength S may be overestimated, or that the plume takes more than 30 minutes to develop a quasi-steady aerosol size distribution with a fully developed accumulation mode.

In contrast with the obvious aerosol perturbation and albedo increase, there is a negligible change in LWP between the track and the surrounding environment after 30 minutes (Fig. 7c). The lack of a strong cloud macrophysical response indicates that the radiative response of the cloud at this time results entirely from the Twomey effect. Despite the shift towards smaller cloud droplets, substantial surface precipitation remains inside the simulated track at this time. Fig. 7(d), shows no real difference in precipitation rate between the track and background. The time lag between the aerosol injection and the visible manifestation of the track in the pseudo-albedo field gives a sense of the timescale for the perturbation of the microphysics via activation. There is an additional delay before changes in cloud properties alter surface precipitation characteristics, as existing rainwater in the column takes some time to sediment out. The narrow band of peak rain rates exceeding 4 mm day^{-1} disappears 20 minutes after visible cloud brightening (50 minutes after injection), and virtually all surface precipitation ceases by hour 9.5.

The aerosol perturbation diffuses slowly over the next hour, broadening the track from 1 km to 3 km by laterally mixing into two additional roll updrafts and diluting MBL depth-averaged aerosol number concentrations within the track to 60–100 mg^{-1}. Peak updraft LWP values diminish within the track 90 minutes after injection but increase in the regions adjacent to the central updraft. This lateral redistribution of cloud water out of the updrafts is likely due to drizzle inhibition. Fig. 7(d) shows essentially no area beneath the central updraft of the track where surface precipitation exceeds 0.25 mm day^{-1} after 90 minutes, as compared to peak rates of ∼4–6 mm day^{-1} under the background updraft cores.

After three hours, the track has spread to 5 km width, and MBL depth-averaged N_a has diluted to 30–60 mg^{-1}. The rough inverse scaling of N_a with lateral dispersion (boundary layer depth is not changing much within this period) suggests that local source and sink terms are of secondary importance compared to the advective redistribution of the original aerosol perturbation within the track; we will examine the aerosol budget of the track more precisely below. LWP and optically thick cloud increase throughout the track, with peak LWPs exceeding 100 g m^{-2}. While surface precipitation begins to recover under the track 150 minutes after injection, the average rain rate in the track remains suppressed, as the maximum rain rate in the track is less than half that of the background despite increasing LWP.

At the end of the simulation, eight hours after the aerosol injection, the track is ∼15 km wide, spanning six distinct updrafts, with LWPs as high as 100–140 g m^{-2}. These large values of LWP coupled with slow declines in N_a (and hence N_d) result in the redevelopment of drizzle and surface precipitation beneath the updrafts in the track.

In contrast with prior LES modeling work of idealized ship tracks in a deeper, open-cell boundary layer (Wang and Feingold, 2009b; Wang et al., 2011), Fig. 7a does not show a suppression of background cloud albedo on the flanks of the track due to an induced secondary circulation. Thus, in this shallow, collapsed boundary layer, the simulated track induces a more significant area-integrated albedo perturbation than those seen in previous studies.

Fig. 8 compares the y-averaged stream function and aerosol fields averaged over hour 15 (the seventh hour after the BaseTrack aerosol injection) in simulations BaseTrack and BaseCtrl. Over hour 15, aerosol-cloud-precipitation feedbacks within the track act to reinforce the roll circulation, while the rolls outside the track (and throughout BaseCtrl) become shallower and weaker as the boundary layer collapses. While this would also tend to strengthen the downdrafts and induce cloud thinning on the edges of the track, this does not seem to reduce albedo there. A possible explanation is that the shift in droplet sizes that has inhibited drizzle and reduced moisture dessication in the updrafts overcomes any tendency for cloud thinning in downdrafts.

5.2.1 Continued evolution of the background state

During the eight hours after aerosol injection, the background environment also evolves significantly, with declines in mean LWP (38%), N_a (34%) and albedo (30%), relative to their hour eight peak. The decline in LWP is due to a loss of cloud water, as the rain water path (RWP) for the background remains approximately 10 g m^{-2} throughout.

To better understand this evolution, we analyze domain-mean statistics for hours 8–16 of the unperturbed control branch, for which there is no track that needs to be removed. Fig. 9 shows profiles of liquid-water potential temperature θ_l, cloud water q_c, N_d, radiative heating rate Q_{RAD}, and resolved buoyancy flux B at hours 8, 12, and 16. As mean N_d rapidly diminishes, the cloud becomes optically thinner. This causes the radiative cooling peak, which initially resides just below cloud top, to broaden and shift deeper into the cloud layer, acting to stabilize the upper MBL, as seen in the progressively shallower region of positive buoyancy flux and less well-mixed θ_l profiles at hours 12 and 16. The combination of weakening updrafts and larger cloud droplet sizes resulting from decreased N_d makes it increasingly difficult to support cloud, which leads to a collapse of the boundary layer, as earlier found in a one-dimensional closure model by Ackerman et al. (1993). Much of the MBL turbulent kinetic energy is shear-driven, but this does not prevent the collapse. The increasingly negative buoyancy flux in the updrafts causes the roll structure to become less coherent and wavelengths to shrink, in agreement with the results of sensitivity studies in Chlond (1992) and Müller and Chlond (1996). For further detail regarding boundary layer roll dynamics and the relative importance of shear and buoyancy, the interested reader is referred to the LES study of Glendening (1996).

5.2.2 Aerosol number budget inside and outside the track

In order to further understand the evolution of the track, we examine the MBL depth-averaged aerosol number budget. The only source is the wind speed dependent surface flux, while autoconversion, accretion, interstitial scavenging, and entrainment dilution (since there is no aerosol above the boundary layer) all act as sinks. All these terms are a function of the local column properties, while advection redistributes aerosol between columns.

In Fig. 10, we examine time series of the area averaged $< N_a >$ budget and source terms inside the background environment (left panel) and ship track (right panel). Grid columns are classified as part of the track if their $< N_a >$ exceeds twice the domain median $< N_a >$ of the unperturbed control branch at the same point in time. The local entrainment rate w_e is calculated using a flux-jump approach (see e.g. Faloona et al., 2005) on 8×8 tiles of grid columns. The entrainment tendency is then calculated as $< N_a > |_{w_e} = w_e \left(N_{aFT} - \langle N_a \rangle \right) / z_i$, where w_e is the entrainment rate, N_{aFT} is the free tropospheric aerosol concentration (zero in this case), and z_i is the inversion height, using coarsened spatial maps of z_i and $< N_a >$.

Accretion is initially the largest component of the loss term in both the background environment and track, with a large contribution from scavenging of interstitial aerosol. For the track, the large initial spike in accretion is due to the activation of many new cloud droplets at the base of updrafts with significant precipitation, initially allowing for large loss of aerosol number. However, the simultaneous increase in N_d drives the cloud droplet distribution towards a smaller mean radius, reduces autoconversion efficiency, and inhibits new drizzle formation. After this brief period of reduced accretion, increased LWP resulting from earlier drizzle suppression begins to enhance precipitation again, with efficient collection of N_d in large-scale updrafts. In the background, both accretion and autoconversion diminish, as the continual reduction in background N_d leaves a smaller available population of droplets to be scavenged by precipitation or to autoconvert into drizzle.

The second largest term is the interstitial scavenging of aerosol by cloud, which increases throughout the simulation in the background environment, but is sharply reduced within the track. This is somewhat counter-intuitive, as the collision efficiency for interstitial scavenging increases with decreasing droplet diameter (e.g. see the appendix of Berner et al., 2013, and references therein). While detailed examination of this effect is beyond the current scope, a possible interpretation is that while the collision efficiency may increase in the track, the reduced sedimentation rate of the smaller cloud dropets decreases the gravitational collection factor in the interstitial scavenging term, causing this term to be smaller in the track compared to the background.

Entrainment is the third largest number sink term within the track. Entrainment dilution rate is initially larger in the track due to an enhanced entrainment rate and the larger aerosol concentration in the boundary layer, since dilution is proportional to the difference between the boundary layer and FT concentrations. As the track broadens with lateral mixing and the aerosol concentration in the track approaches that of the background, dilution weakens and becomes the weakest sink term at the end of the simulation. Outside the track, entrainment (and therefore entrainment dilution) is much weaker, and autoconversion is the third strongest term.

The final sink is due to loss of aerosol number to the sea surface in sedimenting cloud droplets and secondarily in falling raindrops. This term is small but non-negligible and improves budget closure, since the simulated cloud frequently extends to the sea surface (Fig. 5). Within the track, it is small during the first five hours due to the small (and hence slowly falling) cloud droplets. By the end of the simulation, though, the cloud droplets ard more numerous in the track and have become large enough to sediment more efficiently, leading to a larger sedimentation loss than in the background at that time.

5.3 Comparison with observations

The MRF C-130 flew a series of in-cloud and above-cloud transects perpendicular to the track 40 km from the *Sanko Peace*. This distance was estimated by Taylor and Ackerman to be approximately 35 minutes downwind, assuming ship relative winds of 20 m s^{-1}. Taylor and Ackerman (1999) provided detailed analysis of these aircraft observations.

We compare these observations with the simulated ship track. As discussed above, due to uncertainties in the actual aerosol source strength and alignment between the track and background roll structure, it is unrealistic to expect a perfect match in aerosol concentration or track width. For comparison, we examine transects from model output at 40 minutes after the aerosol perturbation is injected, as 3D fields were saved every ten minutes. Note that for this comparison, N_d has units of cm^{-3}.

Fig. 11 compares y-averaged transects of droplet number concentration N_d, effective radius r_e, and albedo A with comparable plots reproduced from Figs. 2, 4 and 5 of Taylor and Ackerman (1999). The x-axis of the original Taylor and Ackerman figures is given in time. Assuming constant heading and 100 m s^{-1} flight speed, each minute covers 6 km, so their transects are 24–30 km in length. The in-cloud leg analyzed by Taylor and Ackerman was flown at 285 m altitude, so the model transects of N_d and r_e are taken from the closest model level (283.75 m). For the N_d transect, the qualitative agreement with the aircraft observation is quite good. Cloud cover at this level is lower than in the observations, resulting in a low bias to the background N_d, but the peaks of 20 cm^{-3} are consistent with observations (the average is not cloud-conditional, as spatial variability and N_d gradients create noise). The track itself is narrower than in the observations at this time, spanning barely 2 km as opposed to 4 km in the transect presented by Taylor and Ackerman. The narrower track width in the model helps explain larger peak concentrations relative to the observations, with the maximum of 178 cm^{-3} significantly in excess of the observed peak of 130 cm^{-3}. However, the average simulated value across a 2 km window including the track is only 67 cm^{-3}, similar to the observed mean of 60 cm^{-3} across the ~4 km wide track.

Taylor and Ackerman (1999) found that drizzle size droplets contributed significantly to the effective radius, as values of r_e determined from in-situ distributions of cloud droplet sized particles were several μm smaller than those retrieved radiometrically, a discrepancy fixed by including drizzle-size droplets in the calculation. A modified effective radius is used within the model to include this effect:

$$r_e = \frac{(q_c + q_r)}{\frac{q_r}{r_{er}} + \frac{q_c}{r_{ec}}}.$$

The observations averaged two-second blocks of data for computing r_e, which is equivalent to a four-gridpoint average in the model framework. In the second panel on the left, the model r_e transect shows a mean of 18 μm within the background and a drop to 10 μm within the track, in excellent agreement with the observations. The representative simulated r_e transect is noisier than the observations, likely in part due to the more broken cloud compared with the observed case, as well as the relatively coarse sampling of the spatial variability of the droplet distribution resulting from the 50 m horizontal grid spacing.

Aircraft albedo observations are not directly comparable with the model output, as they were measured just above cloud top, whereas the model values are for TOA and affected by the overlying atmosphere; thus here our comparison is mainly qualitative. The albedo transect clearly demonstrates the lower overall albedo and more broken nature of the modeled MBL structure. The observed albedo never falls below 0.27, while in several spots the model albedo falls below 0.1. The background peak albedos are broadly consistent at ~0.3 with the observations, suggesting that either evaporation of thin cloud flanking the large scale updrafts is excessive or precipitation is too intense within the model, removing liquid water that would otherwise be available for cloud flanking the updrafts. However, the albedo peak within the model transect of 0.47 yields a comparable increase relative to the background mean as does the observed value of 0.52.

Fig. 12 shows profiles of cloud and rain water conditionally sampled from the track and background at 40, 90 and 420 minutes after track injection, averaged over both updrafts and downdrafts. The rain mixing ratio is scaled by a factor of four for clarity. The background profile of q_l (which includes both cloud and rain water), constructed by Taylor and Ackerman is overplotted in black. The peak in liquid water for the background is located near 210 m, with cloud tops at or slightly above 300 m. Significant rainwater remains in the column at 40 minutes, but decreases are apparent near the top of the profile, as the autoconversion source of new drizzle is diminished with the shift to smaller cloud droplets. This profile is qualitatively consistent with the in-situ measurements, which showed slight increases within the track of liquid water content (LWC) for the instruments most sensitive to cloud size droplets, and slight decreases of LWC for instruments with higher sensitivity to drizzle; this is qualitatively consistent with decreasing q_r and increasing CWP, depending on the cut-off diameters for the respective instruments. After 90 minutes, the peak in cloud water within the track has lifted to 250 m and liquid water content (LWC) has increased by 50% to 0.3 g kg^{-1}, while rainwater in the track has become negligible. After six hours, the peak in track LWC has increased slightly while shifting back downwards to 225 m. Drizzle in the track is recovering towards the background profile, though the background cloud water peak has decreased 20% while shifting downwards to 150 m.

In Fig. 8, a plume of aerosol in the inversion layer is evidently emanating from the shiptrack, due to broadening of the inversion layer above the cloud top due to shear-driven mixing. One transect flown by the C-130 did show an increase in Aitken mode particles above cloud top. The above-cloud aerosol plume was sufficiently surprising in an otherwise pristine environment to be explicitly noted in the flight summary. However, the observed concentrations ($\sim$15 cm^{-3}) were small compared both to those simulated and to the observed cloud droplet concentrations within the track. This is not definitive, as the available data are inadequate to tell how close to cloud top the data were taken, but it appears that more aerosol is detrained in the model than is supported by the observations.

While the simulated track maintains higher cloud tops than the background at 40 minutes after injection, it does not deepen as rapidly or as much as the observationally reported 100 m (Taylor and Ackerman, 1999). One hour after the aerosol perturbation, the difference between cloud tops inside vs. outside the track ranges between 20–30 m. The maximum separation in run BaseTrack between cloud tops in the track and background is 60 m, but this only develops by the end of the simulation and is driven more by the collapse of the background than the continual deepening of the ship track. Fig. 13 shows a Hovmöller plot of the y-averaged entrainment derived using the local flux jump calculations; while averaging in y blurs maxima in the surrounding environment, it is clear that the central circulation in the ship track is entraining air at least twice as rapidly as the background average. Were aerosol concentrations higher just above the entrainment zone than in the boundary layer, this could act as a positive feedback that would accentuate the track. Given the highly elevated aerosol concentrations typical of a ship track, however, it is likely that entrainment is usually a negative feedback that enhances the dilution of track aerosol concentrations, since FT aerosol concentrations larger than the track values are likely rare in the remote MBL.

5.4 Sensitivity of track to relative wind direction

Etling and Brown (1993) noted that the presence of roll structures can have a profound influence on turbulent fluxes within the boundary layer, and that the effective turbulent diffusion can be highly anisotropic. This affects the dispersion of aerosol within shear driven boundary layers. The shear between updrafts and downdrafts of individual rolls tends to diffuse perturbations along them much more rapidly than mixing can transport a scalar between adjacent rolls. In the case of ship tracks, we expect ship tracks with a larger crossing angle relative to the roll axis to spread more rapidly than a track that parallels the roll axis. We tested this using run SensPerp by rotating the geostrophic wind 90° clockwise, such that the ship track is now inserted perpendicular to the rolls rather than parallel to them. This run is spun up for the same initial eight hour period as in BaseSpinup, after which the track is inserted and the run continued for a further six hours. Fig. 14 shows the albedo field for run SensPerp at hours 9, 11, and 13; rapid broadening of the track is readily apparent.

In Fig. 15, the background (blue), track (red), and domain averaged (black) statistics of albedo, $< N_a >$, LWP, and precipitation are shown for SensPerp, BaseTrack, and SensHiAer (to be discussed below). The BaseTrack simulation is shown in the middle panel to facilitate comparison with both sensitivity studies. The fraction of the domain within the track at each time in each run can be inferred from the ratio of vertical distances of the black curve from the blue vs. from the red curve. The initial aerosol pulse is spread much more rapidly in SensPerp than in BaseTrack, indicated by the more rapid decrease of in track $< N_a >$ in Fig. 15, as the aerosol quickly enters all roll cells across the domain and rapidly disperses along the rolls. This suppresses precipitation across a broader area in SensPerp, increasing domain-mean LWP, $< N_a >$, and albedo. However, because the injected aerosol in SensPerp is distributed more broadly than in BaseTrack, the in-track perturbation is smaller, so precipitation more quickly recovers to environmental values.

The larger domain-mean albedo in SensPerp than in BaseTrack can be related to results of Wang et al. (2011). For their case, they found that for a precipitating boundary layer with a low background aerosol concentration, a larger domain-mean albedo increase could be achieved with a uniform aerosol source across the whole domain (loosely analogous to SensPerp, regarding the enhanced lateral mixing as analogous to spreading the original source) than for a single point source (analogous to BaseTrack). In their non-precipitating cases, for a given domain-mean aerosol source, the domain-mean albedo increase was independent of the injection configuration, indicating a more 'linear' regime.

5.5 Simulated track in a polluted environment

In a second sensitivity study SensHiAer, the initial background aerosol concentration is set to 300 mg^{-1}. We also increase the injection aerosol source strength by a factor of 10 compared to the baseline case to make the track stand out clearly against the polluted background. The higher boundary layer aerosol concentration shifts the cloud droplet distribution to smaller sizes, limiting drizzle formation and reducing surface rain rates relative to the BaseTrack case. Reduced precipitation allows for a more turbulent cloud and greater entrainment, leading to boundary layer deepening, a thicker cloud, and larger LWP. During the eight hour spin-up before the aerosol injection, stronger entrainment dilution and cloud processing lead to a decline of $< N_a >$ to 100–120 mg^{-1}, while the boundary layer deepens to $\sim$400 m.

The right column of Fig. 16 shows Hovmöller plots of albedo, $< N_a >$, LWP, and surface precipitation, assembled similarly to Fig. 7. The Twomey effect renders the track visible in the first hour despite the bright surrounding cloud. Comparison of the right two columns of Fig. 15 shows that the track mean albedo gain is less than in clean cases, despite the much stronger aerosol injection, as the background cloud is significantly brighter.

Within the first hour, the LWP in the ship track decreases a few percent below the background, as is commonly observed in Type 2 ship tracks (Coakley and Walsh, 2002; Chen et al., 2012). Entrainment is nearly 40% greater in the ship track vs the background. While the air above the inversion is quite moist (9.2 g kg^{-1} vs 10 g kg^{-1} in the MBL), it is also potentially warmer, so cloud water evaporation due to entrainment warming may promote the in-cloud LWP decrease, consistent with results of Ackerman et al. (2004), Bretherton et al. (2007), and Wood (2007). Alternatively, it is possible that this LWP difference reflects changing in-track contributions from high-LWP updrafts and low-LWP downdrafts of the circulation as the track spreads. The smooth time evolution of the in-track and environmental LWP suggest that their difference is real, rather than an averaging artifact. Once the difference is established, the track and background LWPs reconverge over the next four hours (seen in Fig. 15). While the LWP in both the track and background initially increase at a similar rate during hour nine due to continued cloud deepening, cloud-aerosol feedbacks in the background allow for an increasing precipitation rate, arresting the LWP increase and leading to net loss from the background cloud by hour twelve. By contrast, the elevated aerosol concentratiion in the track largely inhibits precipitation and allows for continued LWP gains, such that the track LWP exceeds that of the background after hour12.5.

Despite significant differences in boundary layer organization and background thermodynamic profile, SensHiAer evolves quite similarly to the high-aerosol case of Wang and Feingold (2009b), which is also in a nearly overcast and non-precipitating cloud regime.

5.6 Attribution of albedo response

In this section, we estimate the contributions of the first and second aerosol indirect effects to the increase of TOA albedo A in the ship track. To do this, we first estimate the 'bulk' albedo A_{bulk} of the cloud-containing layer, including both the fraction f_{cld} of the columns within of that layer that contain cloud, and the clear columns in between. Since the cloud-containing layer is thin, we neglect any clear-sky absorption or scattering within it, so its bulk albedo is due only to its cloudy columns:

$$A_{bulk} = f_{cld} A_{cld} \tag{2}$$

where A_{cld} is the horizontal-average cloud albedo.

We use a simplified model for cloud albedo (e.g. Platnick and Twomey, 1994; Brenguier et al., 2000) as a function of cloud-mean N_d and in-cloud liquid water path W_{cld}:

$$A_{cld} = \frac{(1-g)\tau}{2+(1-g)\tau} \tag{3}$$

$$\tau = C_1 (k N_d)^{1/3} W_{cld}^{5/6} \tag{4}$$

where

$$C_1 = 0.0258\,(f_{ad}\Gamma_{ad})^{-1/6}$$

In eqns. (3) and (4), $g = 0.85$ is the asymmetry factor for light scattering from a small spherical water droplet, $k = 0.8$ is a breadth parameter for the droplet size distribution, f_{ad} is an assumed ratio of the liquid water content profile to its adiabatic value, set to 0.65 in the drizzly low-aerosol runs and 0.9 in the high-aerosol sensitivity case, and $\Gamma_{ad} = 2 \times 10^{-6}$ is a representative rate of adiabatic increase for liquid water content with height, in units of kg kg^{-1} m^{-1}. Using (2), (3) and (4), we can separately estimate A_{bulk} for the track and environment at each time based on their respective mean values of cloud fraction, LWP and N_d. Horizontal cloud heterogeneity and inaccuracies in the assumed vertical structure of the in-cloud liquid water profile in the cloud will lead to errors in these estimates of A_{bulk}.

We use an empirical fit to go from A_{bulk} to TOA albedo A. While we did not store the radiative fluxes for each column of the LES at each time, we did store their domain-mean values, which we use for this fit. Let $SW_\uparrow$ and $SW_\downarrow$ denote the domain-mean downwelling and upwelling shortwave fluxes, and let superscripts $^-$, $^+$ denote fluxes at the cloud base and cloud top. To estimate the bulk albedo from the cloud base and cloud top fluxes, we must consider shortwave radiation impinging on the cloud from below as well as above. We neglect cloud-layer absorption, so a fraction $1 - A_{bulk}$ of the upwelling shortwave radiation at cloud base exits through the cloud top, while by definition a fraction A_{bulk} of the downwelling shortwave radiation at the top of the cloud layer is also reflected upward. After minor algebra, this implies that

$$A_{bulk} = \frac{SW_\uparrow^+ - SW_\uparrow^-}{SW_\downarrow^+ - SW_\uparrow^-} \quad (5)$$

The cloud layer base and top are defined as the bottom and top model levels where domain-mean cloud fraction exceeds 0.05. A scatterplot of domain-mean A_{bulk} vs. A including all output times from both the control and high-aerosol simulations yielded an accurate linear fit,

$$A = 0.69 A_{bulk} + 0.07, \quad (6)$$

which we also use separately for the track and environmental regions. Together with (2), (3) and (4), (6) allows the LES TOA albedo to be predicted from the cloud fraction, LWP and N_d, both inside and outside the track. The empirically-determined intercept, 0.07, which should be the clear-sky albedo, is reassuringly similar to the ocean surface albedo of 0.08.

The top panels of Fig. 17 show the track and background values for A derived from the LES-predicted radiative fluxes and the simplified model in each simulation. The simplified model predicts the evolution of the track and background albedos, and their difference, reasonably accurately, so is useful for decomposing their albedo difference into component contributions.

An approximate linearized decomposition of the response of A_{bulk} into changes due to N_d, f_{cld} and W_{cld} can be used to interpret the albedo response of the boundary layer to the ship track. It is derived from eqns. (2), (3), and (4):

$$\Delta A_{bulk} = \left(\frac{\partial A}{\partial \ln \tau}\right)_{ref}\left(\frac{\Delta \ln N_d}{3} + \frac{5\Delta \ln W_{cld}}{6}\right) + \Delta f_{cld} A_{cld,ref}, \qquad \frac{\partial A}{\partial \ln \tau} = \frac{A_{cld}}{1 - A_{cld}} \quad (7)$$

This is mapped via the linear fit (6) to changes in A. We use the in-track conditions to define the reference state, which makes the linearization more accurate than using the background conditions.

The bottom panels of Fig. 17 apply this decomposition to our three ship track simulations. It captures the magnitude and evolution of the albedo difference predicted by the full idealized model and by the LES radiation code, validating the meaningfulness of this decomposition.

In run BaseTrack, Fig. 17 indicates the initial brightening of the track over the first hour is due primarily to increased N_d (first aerosol indirect effect). Over the next several hours, however, the aerosol perturbation is laterally mixed and subject to various microphysical sinks, diminishing the N_d perturbation. Simultaneously, precipitation suppression in the track induces a steady increase in ΔW_{cld}. By the time the simulation ends at hour 16, the albedo contributions of enhanced N_d and LWP are comparable and when the cloud fraction enhancement in the track is also considered, second indirect effects are more significant to the track albedo perturbation than the first indirect effect. This pattern is repeated in run SensPerp, but here the LWP contribution becomes more rapidly significant.

In contrast, the albedo response of Run SensHiAer is dominated over the entire simulation by the first indirect effect, and the slight decrease of LWP within the track leads to a weakly negative second indirect effect during part of the simulation. In cases with a drier free-troposphere in which enhanced entrainment in the track may lead to a more pronounced decrease of LWP, the albedo in the track can actually be reduced compared to the environment (Chen et al., 2012). Cloud cover is not an important contributor to the second indirect effect in this case, since it remains nearly 100% both inside and outside the track.

The importance of the second aerosol indirect effect in later stages of the SensPerp and Base-Track runs indicates the need to simulate cloud macrophysical responses to aerosol. Similarly, run SensHiAer show that even in a very shallow cloud-topped boundary layer topped by a humid free troposphere, the second indirect effect need not be positive. Suppression of cloud surrounding the track in the simulations of Wang and Feingold (2009b) is another form of negative second indirect effect which does not occur in our simulations due to the different environment. The range of possible effects poses a challenge for parameterization of cloud-aerosol interactions.

6 Ship tracks and aerosol-cloud regimes

Rosenfeld et al. (2006) suggested that closed cell, open cell, and collapsed boundary layer organizations exemplified aerosol-cloud regimes, where the availability of CCN would control boundary layer dynamics via precipitation and feedbacks on turbulence and cloud macrophysical structure, which in turn would modulate the CCN. They proposed that the boundary layer could naturally evolve via cloud-aerosol-precipitation interactions from closed cells to open cells, followed by transition to a collapsed state, but that strong injections of aerosol, such as from ship exhaust, could then reverse the process. Berner et al. (2013) explored the theme of aerosol-cloud regimes using LES, supporting the idea that closed cells, open cells, and collapsed boundary layers are ‘regimes’ in the sense that under steady large-scale forcing, they evolve slowly with little qualitative change in structure over periods of days, with comparatively rapid transitions occasionally occurring between regimes. Do the Type 1 ship tracks simulated in the present work constitute a regime shift from a collapsing state back towards closed cell organization?

A framing of this question appropriate for our simulations is to ask whether, despite horizontal turbulent dilution, the mean microphysical and macrophysical properties within the track keep diverging from the background for an extended period, promoting a long track lifetime. Fig. 15 shows that this is not the case; in BaseTrack, the track-mean cloud and aerosol properties are tending toward the background properties; since runs SensPerp and SensHiAer end at hour 14, the cloud properties have not evolved as much as in BaseTrack, but the approach of aerosol concentration toward the background suggests that cloud properties will eventually follow suit. With free-tropospheric aerosol, it is conceivable that a strong positive aerosol-entrainment feedback could amplify the in-track aerosol and cloud perturbations and foster a much more prominent and long-lived track. Indeed, the west part of Fig. 1 shows several prominent ship tracks in which the in-track cloud albedo remains high well downwind of the track head, despite substantial broadening of the track.

7 Conclusions

In this study, we have for the first time compared an LES with a coupled bulk aerosol scheme to a well-observed ship track. We simulated the *Sanko Peace* ship track from the 1994 MAST field campaign. The track formed in a shallow, low-aerosol boundary layer under high winds. We used a Lagrangian approach, simulating at high resolution a region around the track which evolves with time, corresponding to increasing downstream distance from the ship. Overall, the baseline simulation is quite successful. It compares well to important observed features, including prominent roll organization and microphysical characteristics of the ambient boundary layer, the magnitude of the cloud droplet number enhancement and albedo increase within the track, and the suppression of drizzle.

There are some discrepancies between simulation and observations, including the simulated ambient cloud being more broken than observed, the track being too narrow for its downstream distance from the source, less deepening of the simulated cloud tops in the track, a stronger and more single-layered temperature inversion compared to the observations, and apparently excessive aerosol in the shear-driven mixing layer just above the cloud top. These discrepancies are likely due to some combination of biases in the forcings used to drive the LES and in the aerosol source strength, better alignment of the simulated track along the wind than observed, and possible deficiencies in model physics.

The aerosol concentration in the simulated tracks evolves mainly by lateral dilution (at a rate sensitive to the orientation of the ship to the wind) as the tracks broaden. The wind-driven surface aerosol source is countered by losses mainly due to accretion (which increases with time in the track as the in-track LWP increases) and cloud scavenging of interstitial aerosol (reduced within the track).

Liquid water path is enhanced in the Type 1 tracks, even though they also enhance entrainment of warmer air from aloft. For the simulated Type 2 ship track in a high-aerosol environment, entrainment is again enhanced, and depresses LWP below the background mean for 3.5 hours until the surrounding cloud layer thickens and begins to drizzle, perhaps eventually leading to a transition to a Type 1 behavior.

In our simulated Type 1 tracks, albedo response is initially dominated by the first indirect effect. The second indirect effect becomes increasingly important over time and is responsible for the majority of the albedo perturbation by the end of the simulation. Our sensitivity study of a Type 2 track is dominated by the first indirect effect for the entirety of the six hour run, with a negative second indirect effect for half of that time. Comprehensive ship track observations in a wider range of environments could be used to further test how well the quantitative details of aerosol-cloud interaction are represented by current aerosol models coupled to LES, or other types of process models.

Acknowledgements. Thanks to Marat Khairoutdinov of Stony Brook University for maintaining and providing SAM for use in this study, and to Peter Blossey at UW for assistance with debugging model modifications. Simon Osborne of the UKMO kindly provided the C-130 data from the *Sanko Peace* case. Helfpul conversations with Tom Ackerman and Bryce Harrop improved the manuscript. We would like to gratefully acknowledge support from NSF grants ATM-0745702 and AGS-1242639, the University of Washington College of the Environment Geoengineering Initiative, as well as high-performance computing support from Yellowstone (ark:/85065/d7wd3xhc) provided by NCAR's Computational and Information Systems Laboratory, sponsored by the National Science Foundation.

References

Abdul-Razzak, H. and Ghan, S. J.: A parameterization of aerosol activation: 2. Multiple aerosol types, J. Geophys. Res., 105(D5), 6837–6844, doi:10.1029/1999JD901161, 2000.

Ackerman, A. S., Toon, O. B. and Hobbs, P. V.: Dissipation of marine stratiform clouds and collapse of the marine boundary layer due to the depletion of cloud condensation nuclei by clouds, Science (New York, N.Y.), 262(5131), 226–9, doi:10.1126/science.262.5131.226, 1993.

Ackerman, A. S., Toon, O. B. and Hobbs, P. V.: Numerical modeling of ship tracks produced by injections of cloud condensation nuclei into marine stratiform clouds, J. Geophys. Res., 100(D4), 7121–7133, doi:10.1029/95JD00026, 1995.

Ackerman, A., O. B. Toon, D. E. Stevens, and J. A. Coakley, Jr.,: Enhancement of cloud cover and suppression of nocturnal drizzle in stratocumulus polluted by haze, Geophys. Res. Lett., 30(7), 1381, doi:10.1029/2002GL016634, 2003.

Ackerman, A., M. P. Kirkpatrick, D. E. Stevens, and O. B. Toon: The impact of humidity above stratiform clouds on indirect aerosol climate forcing, Nature, 432, 1014-1017, doi:10.1038/nature03174, 2004.

Albrecht, B. A.: Aerosols, Cloud Microphysics, and Fractional Cloudiness, Science, 245(4923), 1227–1230, doi:10.1126/science.245.4923.1227, 1989.

Baker, M. B. and Charlson, R. J.: Bistability of CCN concentrations and thermodynamics in the cloud-topped boundary layer, Nature, 345(6271), 142–145, doi:10.1038/345142a0, 1990.

Berner, A. H., Bretherton, C. S., Wood, R. and Muhlbauer, A.: Marine boundary layer cloud regimes and POC formation in a CRM coupled to a bulk aerosol scheme, Atmos. Chem. Phys., 13(24), 12549–12572, doi:10.5194/acp-13-12549-2013, 2013.

Blossey, P. N. and Durran, D. R.: Selective monotonicity preservation in scalar advection, J. Comp. Phys., 227(10), 5160–5183, doi:10.1016/j.jcp.2008.01.043, 2008.

Brenguier, J.-L., Pawlowska, H., Schüller, L., Preusker, R., Fischer, J. and Fouquart, Y.: Radiative Properties of Boundary Layer Clouds: Droplet Effective Radius versus Number Concentration, J. Atmos. Sci., 57(6), 803–821, doi:10.1175/1520-0469(2000)057<0803:RPOBLC>2.0.CO;2, 2000.

Bretherton, C. S., Blossey, P. N., and Uchida, J.: Cloud droplet sedimentation, entrainment efficiency, and subtropical stratocumulus albedo, Geophys. Res. Lett., 34, L03813, doi:10.1029/ 2006GL027648, 2007.

Bretherton, C. S., Blossey, P. N., and Uchida, J.: Slow manifolds and multiple equilibria in stratocumulus-capped boundary layers, J. Adv. Model. Earth Syst., 2, 14, doi:10.3894/JAMES.2010.2.14, 2010.

Chen, Y.-C., Christensen, M. W., Xue, L., Sorooshian, a., Stephens, G. L., Rasmussen, R. M. and Seinfeld, J. H.: Occurrence of lower cloud albedo in ship tracks, Atmos. Chem. Phys., 12(17), 8223–8235, doi:10.5194/acp-12-8223-2012, 2012.

Chlond, A.: Three-dimensional simulation of cloud street development during a cold air outbreak, Bound.-Layer Meteor., 58(1-2), 161–200, doi:10.1007/BF00120757, 1992.

Christensen, M. W. and Stephens, G. L.: Microphysical and macrophysical responses of marine stratocumulus polluted by underlying ships: Evidence of cloud deepening, J. Geophys. Res., 116(D3), D03201, doi:10.1029/2010JD014638, 2011.

Christensen, M. W. and Stephens, G. L.: Microphysical and macrophysical responses of marine stratocumulus polluted by underlying ships: 2. Impacts of haze on precipitating clouds, J. Geophys. Res., 117(D11), D11203, doi:10.1029/2011JD017125, 2012.

Clarke, A. D., Owens, S. R. and Zhou, J.: An ultrafine sea-salt flux from breaking waves: Implications for cloud condensation nuclei in the remote marine atmosphere, J. Geophys. Res., 111(D6), 1–14, doi:10.1029/2005JD006565, 2006.

Coakley, J. A, Bernstein, R. L. and Durkee, P. A.: Effect of ship-stack effluents on cloud reflectivity., Science, 237(4818), 1020–2, doi:10.1126/science.237.4818.1020, 1987.

Coakley, J. A. and Walsh, C. D.: Limits to the Aerosol Indirect Radiative Effect Derived from Observations of Ship Tracks, J. Atmos. Sci., 59(3), 668–680, doi:10.1175/1520-0469(2002)059¡0668:LTTAIR¿2.0.CO;2, 2002.

Conover, J. H.: Anomalous Cloud Lines, J. Atmos. Sci., 23(6), 778–785, doi:10.1175/1520-0469(1966)023¡0778:ACL¿2.0.CO;2, 1966.

Deardorff, J.: Stratocumulus-capped mixed layers derived from a three-dimensional model, Bound.-Layer Meteor., 18, 495-527, 1980.

Dee, D. P., Uppala, S. M., Simmons, A. J., Berrisford, P., Poli, P., Kobayashi, S., Andrae, U., Balmaseda, M. A., Balsamo, G., Bauer, P., Bechtold, P., Beljaars, A. C. M., van de Berg, L., Bidlot, J., Bormann, N., Delsol, C., Dragani, R., Fuentes, M., Geer, A. J., Haimberger, L., Healy, S. B., Hersbach, H., Hólm, E. V., Isaksen, L., Kållberg, P., Köhler, M., Matricardi, M., McNally, A. P., Monge-Sanz, B. M., Morcrette, J.-J., Park, B.-K., Peubey, C., de Rosnay, P., Tavolato, C., Thépaut, J.-N. and Vitart, F.: The ERA-Interim reanalysis: configuration and performance of the data assimilation system, Q. J. R. Meteorol. Soc., 137(656), 553–597, doi:10.1002/qj.828, 2011.

Durkee, P. A., Noone, K. J. and Bluth, R. T.: The Monterey Area Ship Track Experiment, J. Atmos. Sci., 57(16), 2523–2541, doi:10.1175/1520-0469(2000)057¡2523:TMASTE¿2.0.CO;2, 2000.

Durkee, P. A., Chartier, R. E., Brown, A., Trehubenko, E. J., Rogerson, S. D., Skupniewicz, C., Nielsen, K. E., Platnick, S. and King, M. D.: Composite Ship Track Characteristics, J. Atmos. Sci., 57(16), 2542–2553, doi:10.1175/1520-0469(2000)057¡2542:CSTC¿2.0.CO;2, 2000.

Etling, D., and Brown, R. A.: Roll vortices in the planetary boundary layer: A review. Bound.-Lay. Meteorol., 65(3), 215-248, doi:10.1007/BF00705527, 1993.

Faloona, I., Lenschow, D., Campos, T., Stevens, B., vanZanten, M., Blomquist, B., Thornton, D., Bandy, A., and Gerber, H.: Observations of entrainment in Eastern Pacific marine stratocumulus using three conserved scalars, J. Atmos. Sci, 62, 3268–3285, doi:10.1175/JAS3541.1, 2005.

Ferek, R. J., Hegg, D. a., Hobbs, P. V., Durkee, P. and Nielsen, K.: Measurements of ship-induced tracks in clouds off the Washington coast, J. Geophys. Res., 103(D18), 23199–23206, doi:10.1029/98JD02121, 1998.

Glendening, J. W.: Lineal Eddy Features under Strong Shear Conditions, J. Atmos. Sci., 53(23), 3430–3449, doi:10.1175/1520-0469(1996)053<3430:LEFUSS>2.0.CO;2, 1996.

Hindman, E., Porch, W., Hudson, J. and Durkee, P.: Ship-produced cloud lines of 13 July 1991, Atmos. Environ., 28(20), 3393–3403, doi:10.1016/1352-2310(94)00171-G, 1994.

Hobbs, P. V., Garrett, T. J., Ferek, R. J., Strader, S. R., Hegg, D. A., Frick, G. M., Hoppel, W. A., Gasparovic, R. F., Russell, L. M., Johnson, D. W., O'Dowd, C., Durkee, P. A., Nielsen, K. E. and Innis, G.: Emissions from Ships with respect to Their Effects on Clouds, J. Atmos. Sci., 57(16), 2570–2590, doi:10.1175/1520-0469(2000)057<2570:EFSWRT>2.0.CO;2, 2000.

Khairoutdinov, M. F. and Kogan, Y. L.: A new cloud physics parameterization in a large-eddy simulation model of marine stratocumulus, Mon. Weather Rev., 128(1), 229–243, doi:10.1175/1520-0493(2000)128<0229:ANCPPI>2.0.CO;2, 2000.

Khairoutdinov, M.F. and Randall, D. A.: Cloud resolving modeling of the ARM summer 1997 IOP: Model formulation, results, uncertainties, and sensitivities, J. Atmos. Sci., 60, 607-625, 2003.

Liou, K. N. and Ou, S.C.: The role of cloud microphysical processes in climate: An assessment from a one-dimensional perspective, J. Geophys. Res., 94(D6), 2156-2202, doi:10.1029/JD094iD06p08599, 1989.

Mlawer, E. J., Taubman, S. J., Brown, P. D., Iacono, M. J. and Clough, S. A.: Radiative transfer for inhomogeneous atmospheres: RRTM, a validated correlated-k model for the longwave, J. of Geophys. Res., 102(D14), 16663, doi:10.1029/97JD00237, 1997.

Moeng, C.-H. and Sullivan, P. P.: A Comparison of Shear- and Buoyancy-Driven Planetary Boundary Layer Flows, J. Atmos. Sci., 51(7), 999–1022, doi:10.1175/1520-0469(1994)051<0999:ACOSAB>2.0.CO;2, 1994.

Morrison, H., Curry, J. A. and Khvorostyanov, V. I.: A new double-moment microphysics parameterization for application in cloud and climate models. Part I: Description, J. Atmos. Sci., 62(6), 1665–1677, doi:10.1175/JAS3446.1, 2005.

Morrison, H. and Grabowski, W. W.: Modeling supersaturation and subgrid-scale mixing with two-moment bulk warm microphysics, J. Atmos. Sci., 65(3), 792–812, doi:10.1175/2007JAS2374.1, 2008.

Müller, G., and Chlond, A.: Three-dimensional numerical study of cell broadening during cold-air outbreaks. Bound.-Lay. Meteor., 81(3-4), 289-323, doi:10.1007/BF02430333, 1996.

Platnick, S. and Twomey, S.: Determining the Susceptibility of Cloud Albedo to Changes in Droplet Concentration with the Advanced Very High Resolution Radiometer, J. Appl. Meteorol., 33(3), 334–347, doi:10.1175/1520-0450(1994)033¡0334:DTSOCA¿2.0.CO;2, 1994.

Radke, L. F., Coakley, J. a and King, M. D.: Direct and remote sensing observations of the effects of ships on clouds., Science, 246(4934), 1146–9, doi:10.1126/science.246.4934.1146, 1989.

Rosenfeld, D., Kaufman, Y. J. and Koren, I.: Switching cloud cover and dynamical regimes from open to closed Benard cells in response to the suppression of precipitation by aerosols, Atmos. Chem. Phys., 6(1), 1179–1198, doi:10.5194/acpd-6-1179-2006, 2006.

Schubert, W. H., Wakefield, J. S., Steiner, E. J. and Cox, S. K.: Marine stratocumulus convection. Part I: Governing equations and horizontally homogeneous solutions, J. Atmos. Sci., 36, 1286–1307, 1979.

Stevens, B. and Feingold, G.: Untangling aerosol effects on clouds and precipitation in a buffered system, Nature, 461, 607–613, doi:10.1038/nature08281, 2009.

Taylor, J. P. and Ackerman, A. S.: A case-study of pronounced perturbations to cloud properties and boundary-layer dynamics due to aerosol emissions, Q. J. R. Meteorol. Soc., 125(559), 2643–2661, doi:10.1002/qj.49712555915, 1999.

Twomey, S.: The influence of pollution on the shortwave albedo of clouds, J. Atmos. Sci., 34, 1149–1152, 1977.

Wang, H. and Feingold, G.: Modeling mesoscale cellular structures and drizzle in marine stratocumulus. Part II: The microphysics and dynamics of the boundary region between open and closed cells, J. Atmos. Sci., 66, 3257-3275, 2009.

Wang, H., Rasch, P. J. and Feingold, G.: Manipulating marine stratocumulus cloud amount and albedo: a process-modelling study of aerosol-cloud-precipitation interactions in response to injection of cloud condensation nuclei, Atmos. Chem. Phys., 11(9), 4237–4249, doi:10.5194/acp-11-4237-2011, 2011.

Wood, R.: Cancellation of Aerosol Indirect Effects in Marine Stratocumulus through Cloud Thinning, J. Atmos. Sci., 64(7), 2657–2669, doi:10.1175/JAS3942.1, 2007.

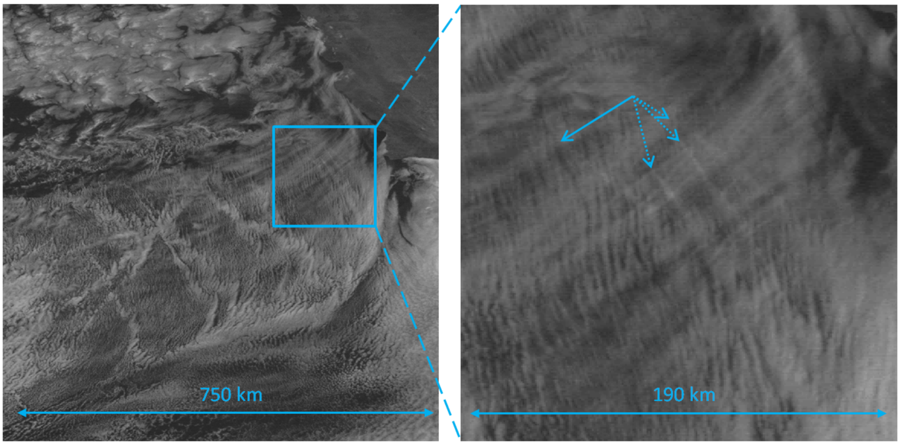

Fig. 1. GOES satellite imagery of the East Pacific near California at 2013UTC on July 13, 1994. A number of ship tracks are clearly visible well off shore. The right panel gives an enlarged view of clouds to the south west of Monterey; despite cirrus obscuring the view, several tracks are apparent, indicated with arrows. The solid arrow marks the estimated location of the *Sanko Peace* at the time of the image.

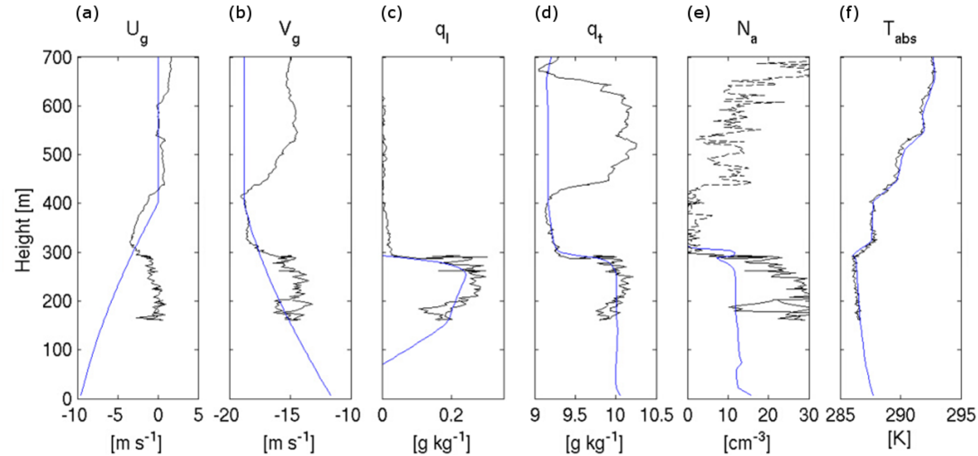

Fig. 2. Background profiles of the wind components u and v, liquid water mixing ratio q_l, total water mixing ratio q_t, absolute temperature T_{abs}, and total aerosol number concentration N_a (the sum of cloud droplet number concentration N_d, rain droplet number concentration N_r, and interstitial aerosol number concentration N_{ad}) observed by the MRF C-130 prior to sampling the *Sanko Peace* ship track (black curves). Overlaid are profiles of the forced geostrophic wind components U_g and V_g, as well as the initial profiles of q_t and T (blue curves).

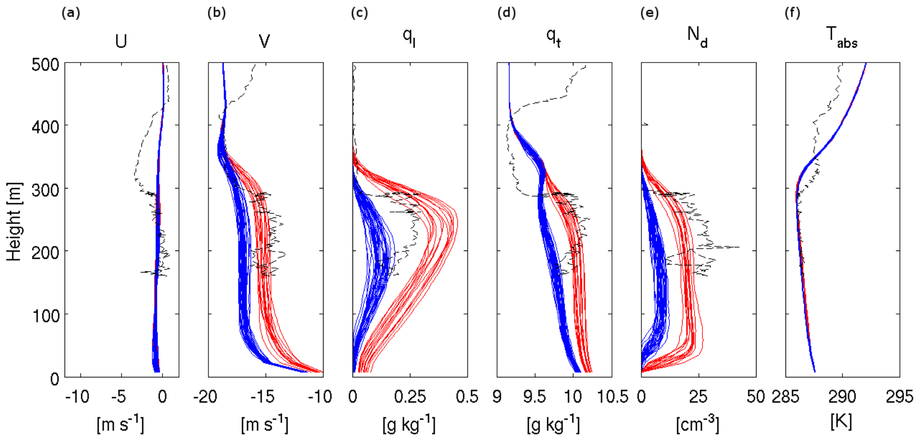

Fig. 3. Profiles of y-averaged u and v winds, liquid water mass mixing ratio q_l, total water mass mixing ratio q_t, absolute temperature T_{abs}, and cloud droplet concentration N_d after eight hours, immediately before the ship track perturbation is introduced. Profiles are sampled at the locations of mesoscale updrafts (red curves) and downdrafts (blue curves), identified by maxima or minima in the y-averaged liquid water path.

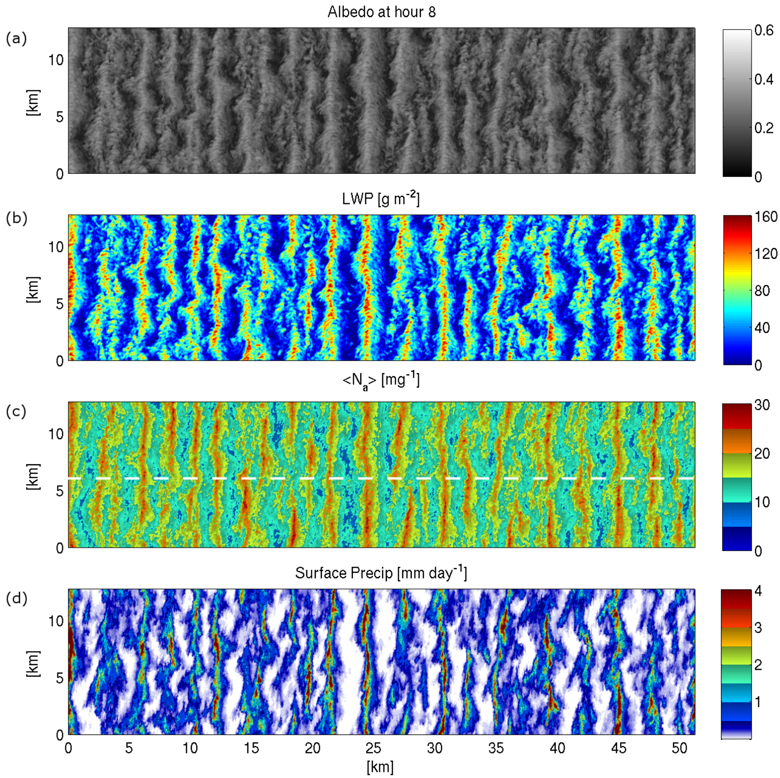

Fig. 4. $x-y$ snapshots of domain (a) albedo A, (b) liquid water path (LWP), (c) total aerosol number concentration $< N_a >$, where brackets denote an average through the boundary layer depth, and (d) surface precipitation rate (0.05 mm day^{-1} threshold) for run BaseTrack at hour 8.

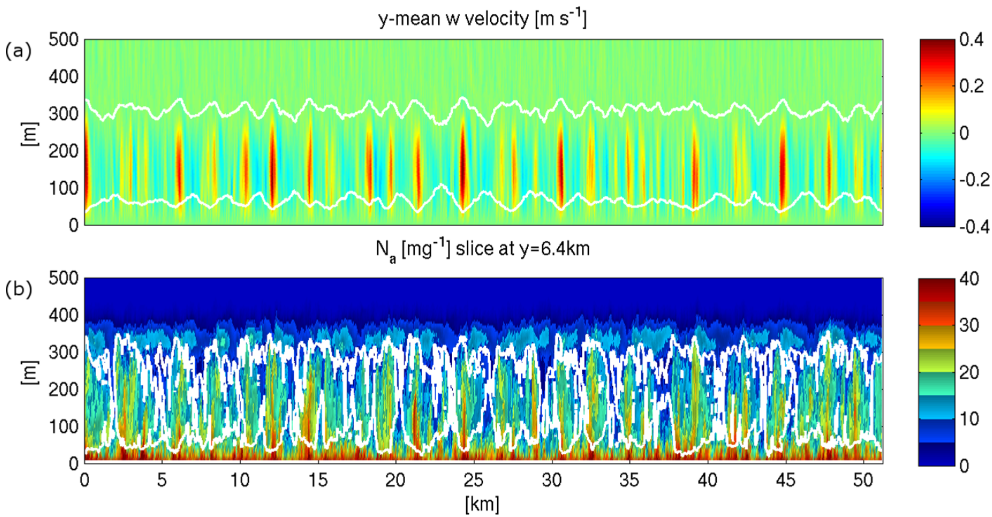

Fig. 5. $x-z$ snapshots of (a) y-averaged vertical velocity w and (b) vertical slice of total aerosol number concentration N_a at y =6.4 km for run BaseTrack at hour 8. White contours mark the 0.01 g kg^{-1} cloud water mixing ratio boundary. Differences in contour appearance result from y-average applied to the fields in panel (a).

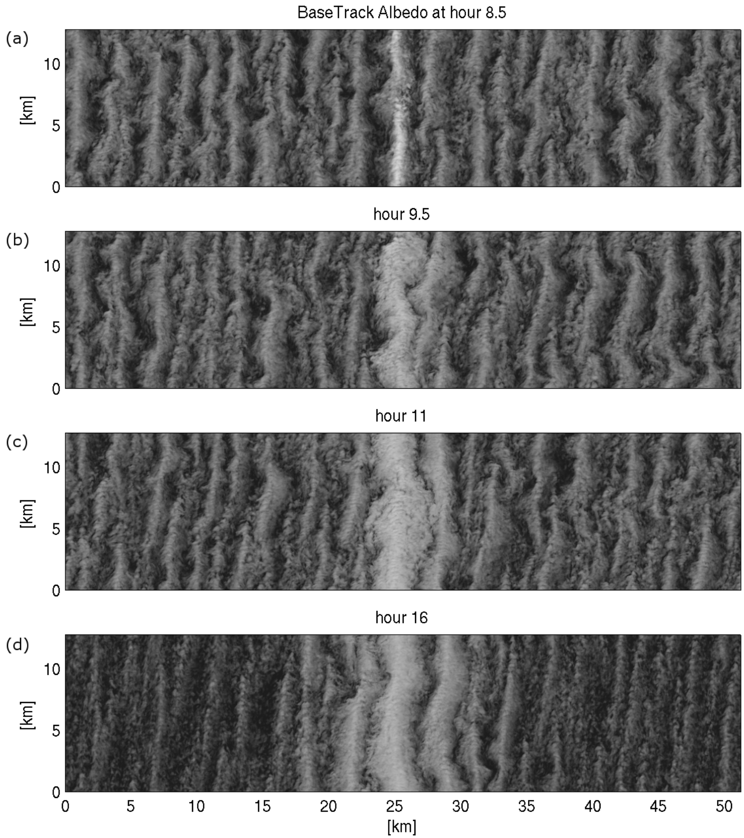

Fig. 6. $x-y$ snapshots of albedo for run BaseTrack at hours (a) 8.5 (half an hour after track injection), (b) 9.5, (c) 11, and (d) 16.

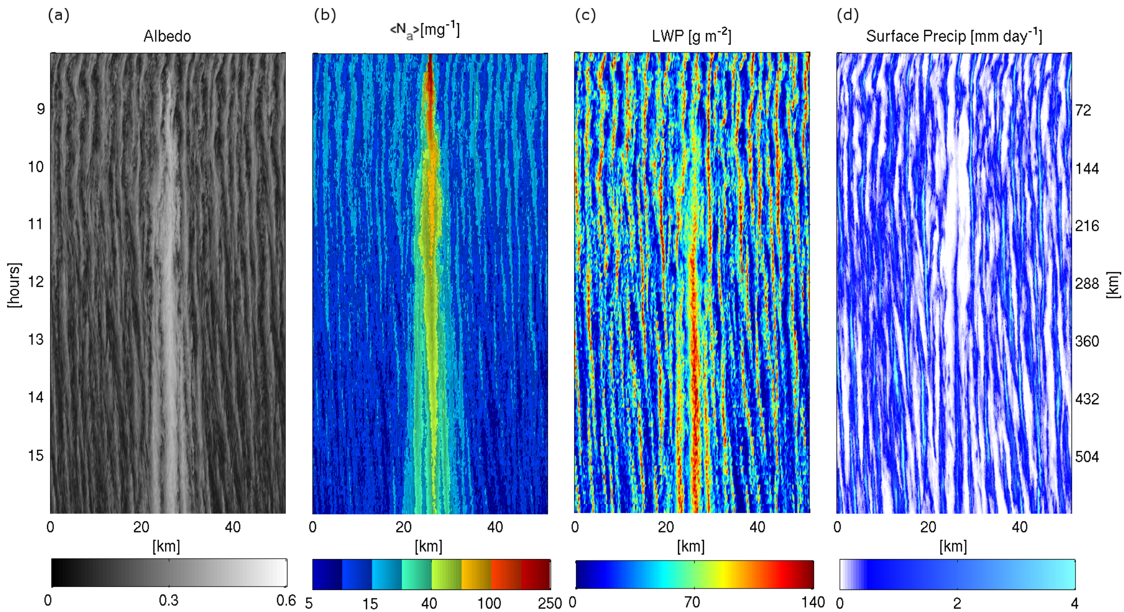

Fig. 7. $x-t$ Hovmöller plots for run BaseTrack of (a) A, (b) $< N_a >$, where brackets denote a column average through the depth of the MBL, (c) LWP, and (d) surface precipitation rate. The axis on the right-hand side of the albedo plot shows the equivalent downstream distance from the ship.

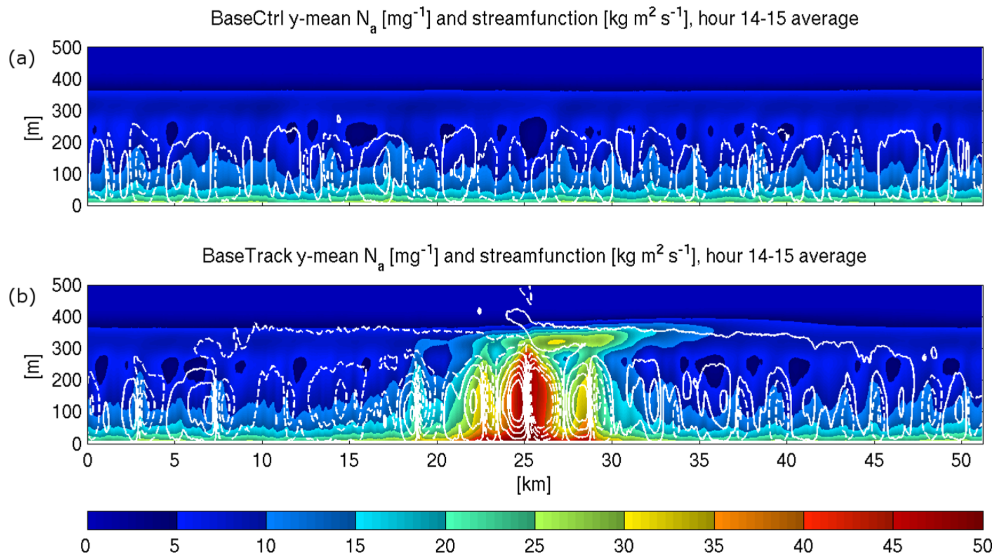

Fig. 8. $x-z$ slice of y-averaged aerosol concentration N_a and y-averaged streamfunction ψ for runs (a) BaseCtrl and (b) BaseTrack in a mean over hour 14 to 15, the seventh hour after track injection. Positive streamfunction (solid white contours) indicates a counterclockwise circulation, while negative streamfunction (dashed contours) indicates a clockwise circulation. Contours shown have magnitudes of $\pm$ 5, 20, 35, 50, 65 kg m^2 s^{-1}.

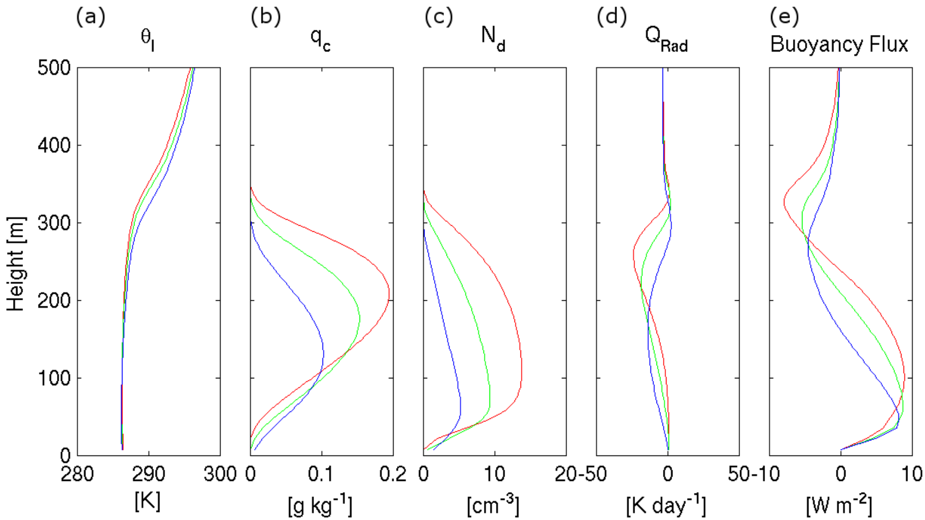

Fig. 9. Domain average profiles from run BaseCtrl for (a) liquid-water potential temperature θ_l, (b) cloud water q_c, (c) cloud droplet number concentration N_d, (d) radiative heating rate Q_{RAD}, and (e) resolved buoyancy flux B. Times shown are for hours 8 (red), 12 (green), and 16 (blue).

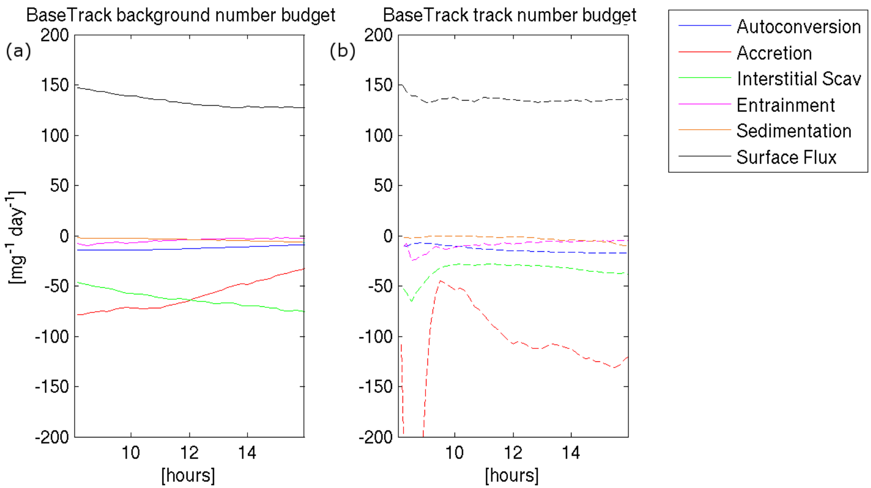

Fig. 10. Regional aerosol budgets for run BaseTrack. (a) Time series of budget term magnitude in the background (solid) and (b) within the ship track (dashed).

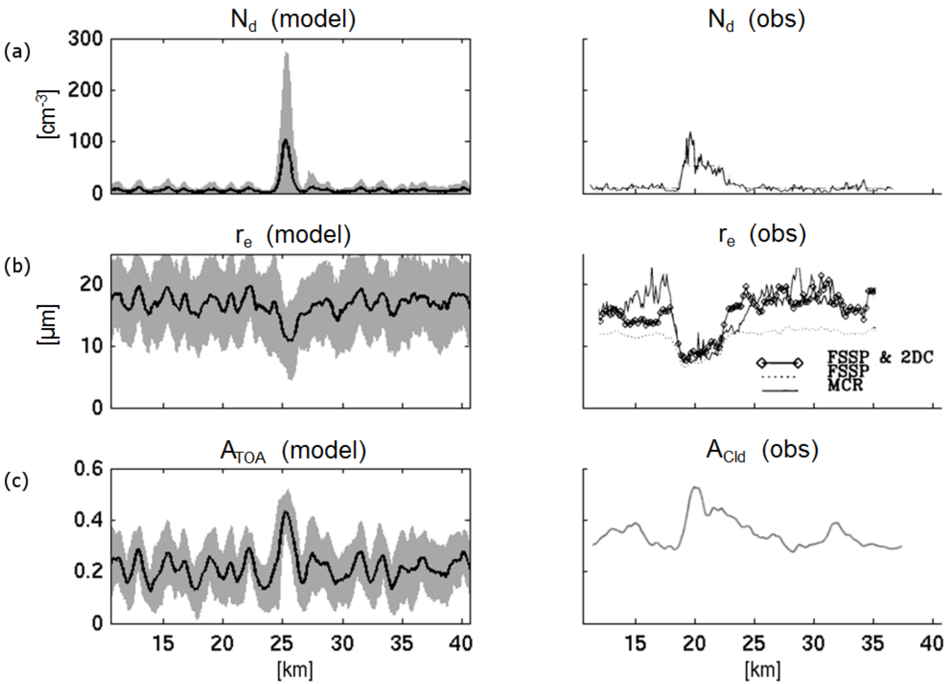

N_d (model)
N_d (obs)
(a)
300
200
100
0
[cm-3]
r_e (model)
r_e (obs)
(b)
20
10
0
[μm]
FSSP & 2DC
FSSP
MCR
A_TOA (model)
A_Cld (obs)
(c)
0.6
0.4
0.2
0
15
20
25
30
35
40
[km]

Fig. 11. Model transects at hour 8.7 of (a) N_d, (b) r_e, and (c) albedo. We compare the modeled top of atmosphere albedo (A_{TOA}) with the observed cloud albedo (A_{Cld}, as the 3d fields for radiative fluxes were not saved and thus computing a modeled cloud albedo is not possible. In each panel, the heavy black curve is the domain y-average, and the grey-filled region is bounded by $\pm 2\sigma$ about the mean, where σ is calculated at each x as the square root of the variance of all values in y. Observations from Taylor and Ackerman (1999) Figs. 2, 4, and 5 are reproduced in the right hand column. The model transects are shown for the time that most nearly corresponds with the observed transects in terms of downstream evolution after aerosol perturbation (about 40 minutes).

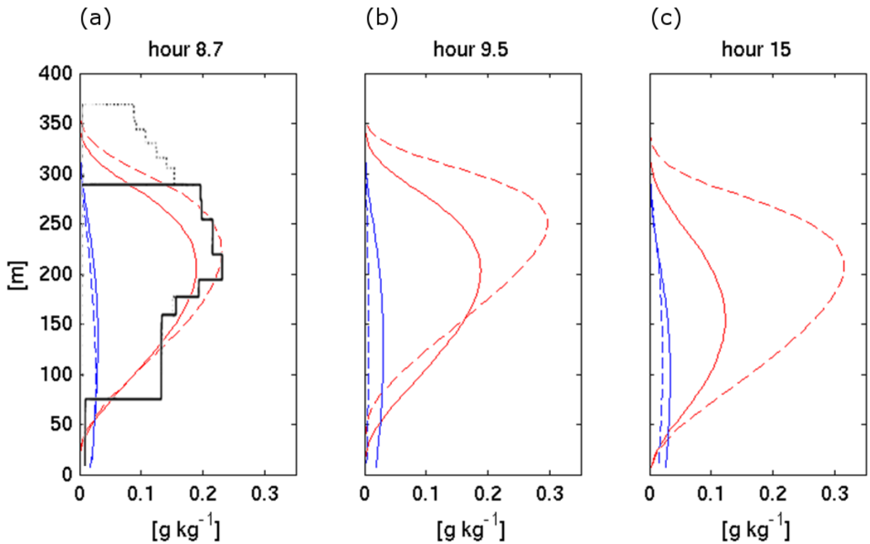

Fig. 12. Profiles of cloud (red lines) and rain (multiplied by factor of four for clarity; blue lines) water mass mixing ratios, regionally averaged in the ship track (dashed lines) and background (solid lines) in run BaseTrack. Plots are shown for hours (a) 8.7, (b) 9.5, and (c) 15. Black overlay in (a) is the composited observational profile for q_l from Taylor and Ackerman (1999).

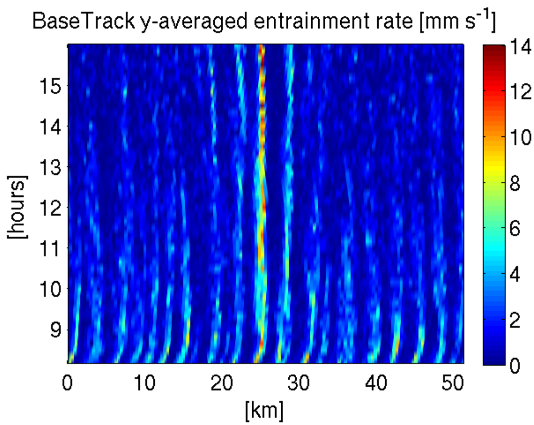

Fig. 13. Hovmöller plot of y-averaged entrainment rate w_e for run BaseTrack.

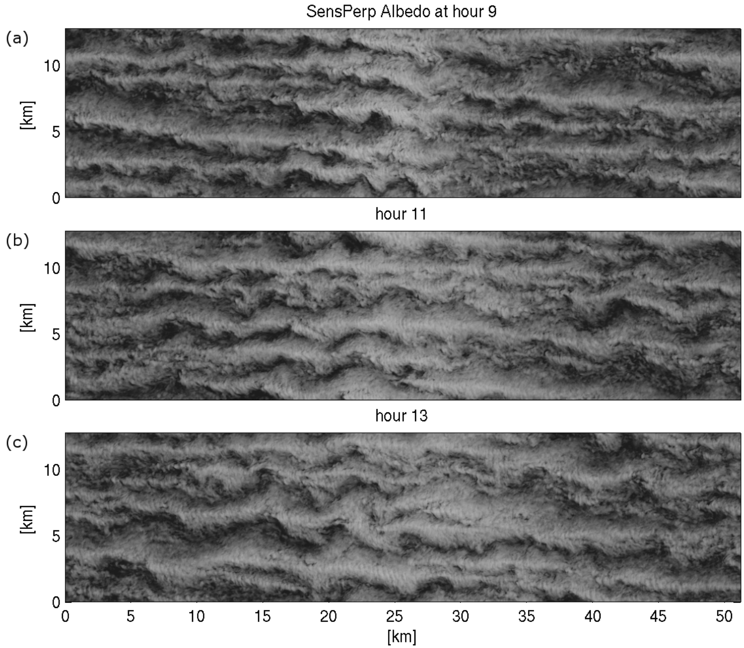

Fig. 14. $x-y$ snapshots of albedo for run SensPerp at hours (a) 9, (b) 11, and (c) 13 (one, three, and five hours after the ship track perturbation is introduced).

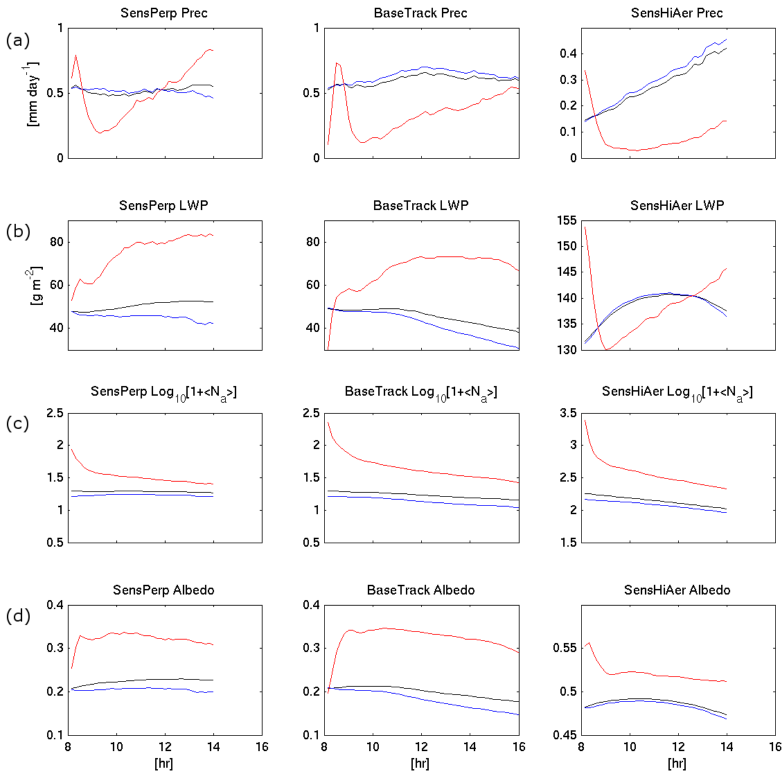

Fig. 15. Track (red line), background (blue line), and domain (black line) averaged time series for runs SensPerp (first column), BaseTrack (second column), and SensHiAer (third column). Plotted are (a) surface precipitation rate, (b) LWP, (c) $< N_a >$, and (d) albedo.

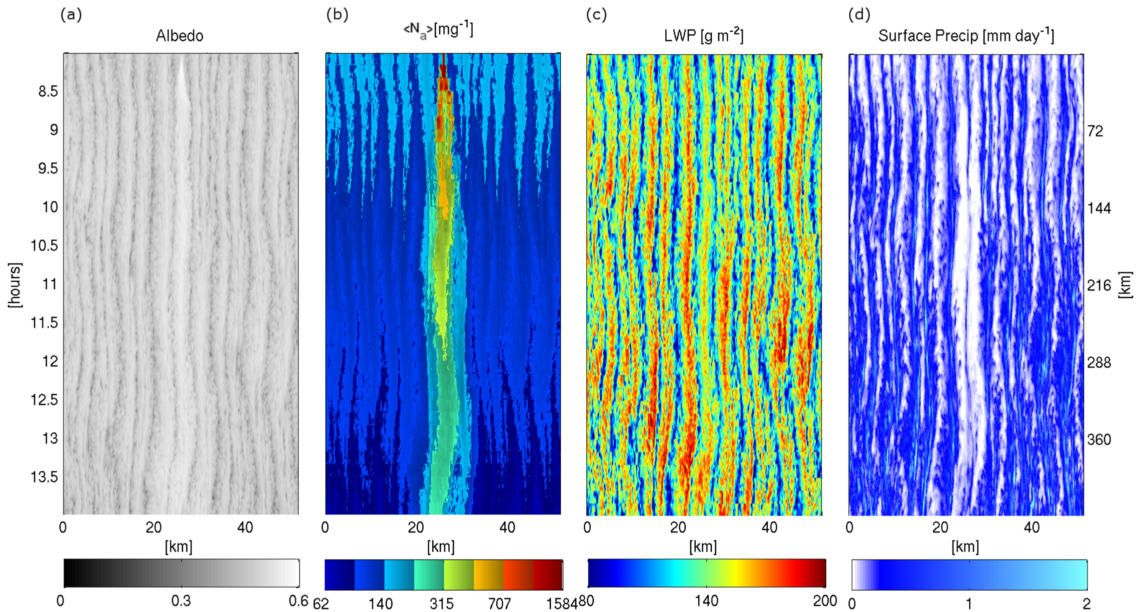

Fig. 16. $x - t$ Hovmöller plot for run SensHiAer; panels as in Fig. 7.

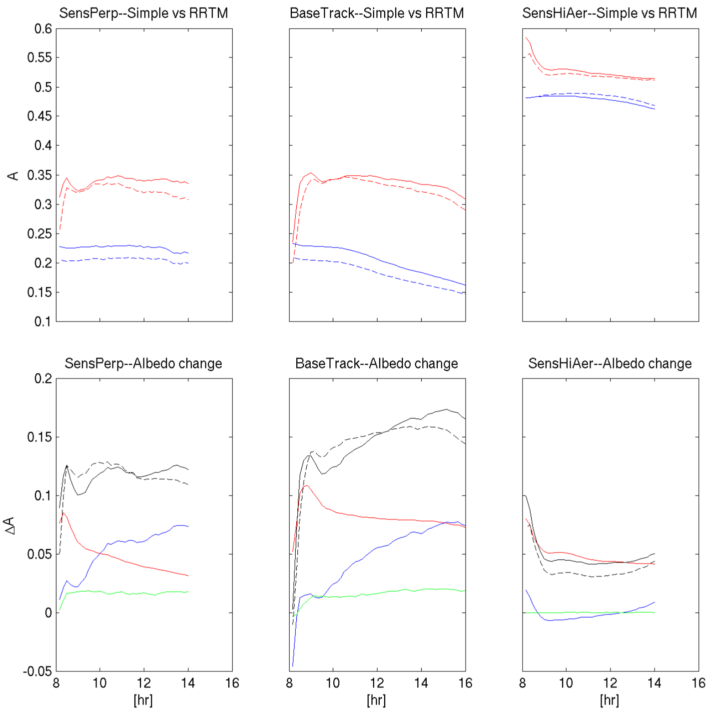

Fig. 17. Top row: simple model (solid lines) and Rapid Radiative Transfer Model (RRTM; dashed lines) predicted A for the track (red lines) and background (blue lines) inr runs SensPerp (first column), Base-Track (second column), and SensHiAer (third column). Bottom row: Albedo change due to changes of N_d (red lines), W_{cld} (blue lines), and f_c (green lines), as well as total predicted change ΔA by the sum of terms (solid black lines) and derived from RRTM (dashed black lines). Runs are as in top row.